7-2017

A Case Study in Basement and Surface Structure Relationships and Their Implications for Fault Reactivation, Sawtooth Range, MT

Jason M. Palu
University of Nebraska-Lincoln, jp22ace@gmail.com

A CASE STUDY IN BASEMENT AND SURFACE STRUCTURE RELATIONSHIPS AND THEIR IMPLICATIONS FOR FAULT REACTIVATION, SAWTOOTH RANGE, MT

by

Jason M Palu

A Thesis

Presented to the Faculty of

The Graduate College at the University of Nebraska

In Partial Fulfillment of Requirements

For the Degree of Master of Science

Major: Earth and Atmospheric Sciences

Under the Supervision of Professor Caroline M Burberry

Lincoln, Nebraska

July, 2017

A CASE STUDY IN BASEMENT AND SURFACE STRUCTURE RELATIONSHIPS AND THEIR IMPLICATIONS FOR FAULT REACTIVATION, SAWTOOTH RANGE, MT

Jason Michael Palu, M.S.

University of Nebraska, 2017

Advisor: Caroline M. Burberry

The reactivation of pre-existing basement structures affects the geometry of subsequent deformation structures. A case study analyzing the results of these interactions can be used to examine multiple fold-thrust systems and lead to valuable deformation predictions. These predictions include the potential for hydrocarbon traps or seismic risk in an actively deforming area. This case study examined the development of structures close to the Augusta Syncline in the Sawtooth Range, Montana (USA), using: 1) an ArcGIS map of basement structures, based on analysis of gravimetric and aeromagnetic data, seismic data, and well logs; 2) an ArcGIS map of the surface deformation structures of the belt, based on interpretation of remote sensing images and verification through the collection of surface field data indicating stress directions and age relationships; 3) analog sandbox experiments established and completed under controlled circumstances; and 4) a comparison of the remote sensing and field data with respect to results from the sandbox models. This comparison was then applied to the Sawtooth Range to better understand its development. Thrust faults in the Sawtooth Range change orientation from NNW-SSE in the north near the Gibson Reservoir to a WNW-ESE orientation near

Haystack Butte. The change in orientation of these thrust faults correlates with pre-existing deformation structures within the Great Falls Tectonic Zone; the Scapegoat-Bannatyne trend within this Zone coincides with the change in orientation. Locally the Scapegoat-Bannatyne trend may be composed of up to 4 NE-SW oriented *en echelon* basement faults. These faults are most likely reactivated sinistral strike-slip faults; the observed up-dip transport direction is W to E. This indicates that the pre-existing basement features have a profound effect on the geometry of the later deformation. The case study's main potential lies in developing a better understanding of the seismic hazard and hydrocarbon pool locations in the study area and it's vicinity and how they were influenced by pre-existing basement faults.

TABLE OF CONTENTS

ACKNOWLEDGEMENTS

First, I much express my deepest gratitude for all the assistance provided by my thesis advisor, Dr. Caroline M. Burberry of the University of Nebraska-Lincoln. She provided me with the much needed inspiration to complete this project and stuck it out with me to the end. This paper is a direct reflection of my time and knowledge gained working under her tutelage. I would also like to thank the University of Nebraska-Lincoln for the use of their facilities and resources, and my committee members Dr. Chris Fielding and Dr. Richard Kettler. Without them, this study would not have been possible. As for assistance with the project, special thanks to Jacob Bruihler for his help completing the field work, and Amanda Jones for her help in the lab.

Finally, none of this would have been possible without the unending support of my parents, and my wife Becky. They were there for me through it all, the ups and downs, and the thick and thin. This accomplishment is theirs as much as it is mine. Thank you all.

INTRODUCTION

The reactivation potential of pre-existing basement structures affects the geometry of subsequent deformation structures. This case study will show that these interactions can be used to predict features of multiple fold-thrust systems, such as variations in surface trend orientation and basement fault reactivation, and lead to valuable deformation predictions. These predictions include the potential for seismic hazard and possible locations of hydrocarbon traps within a fold-thrust system. This case study is the result of an analysis of fold-thrust deformation structures within the Sawtooth Range, Montana.

There is consensus that basement structures do have an effect on subsequent deformation resulting from fault reactivation (Holl & Anastasio, 1992; Koyi & Petersen, 1993; Boyer, 1995; Higgins & Harris, 1997; Harper et al., 2001; Hessami et al., 2001; Boyce & Morris, 2002; Foster et al., 2006; Maillot & Koyi, 2006; Ahmadhadi et al., 2007; Aktepe et al., 2008; Burberry et al., 2011; Hengmao & Yin, 2011; Miller & Mitra, 2011; Fuentes et al., 2012; Leclere & Fabbri, 2013; Burberry, 2015; Burberry & Swiatlowski, 2016). Subsequent deformations are categorized by different deformation regimes that occur after the initial deformation event has concluded. Various causes for reactivation exist, unique to each particular initial and subsequent event. In Anderson's Theory of faulting, a thrust fault system is categorized by σ_1 (maximum compression and least tension) being in the horizontal direction and σ_3 (maximum tension and least compression) being in the vertical (Anderson, 1905). Although Anderson's theory tends

to be applicable to conjugate fault systems, it does not reproduce the behavior of all fault systems. His theory considers mainly the stress conditions at fault nucleation (Healy et al., 2012). He failed, however, to consider the effect of pre-existing faults, with potential for reactivation, and other structures (Healy et al., 2012) and how this affects fault growth and orientation. Most importantly, Anderson's theory applies to fault systems undergoing homogenous stresses, and does not consider polyphase stresses (Healy et al., 2012). In order to provide acceptable predictions for fault reactivation and seismic risk, more factors must be taken into consideration. Fracture size, shape, and densities have direct impacts on the fluid transport capabilities of said rock (Healy et al., 2012). Determining of stress application can also be determined by knowledge of the fault's attitude and location in the medium (Hafner, 1951). These can be reactivated with optimal shear orientations, or cause additional sets of arrays to form and have a linking effect on the system (Scholz, 1989). Aktepe et al. (2008) used seismic velocity models and poststack migration imaging to identify subsurface faulting and collapse due to rhombochasms (a basin that is rhomboid in shape) in the crust resulting from transverse faulting in the Fort Worth Basin in northern Texas. Mapped aeromagnetic and gravity lineament data taken in Ontario, led to a tectonic inheritance model that demonstrated pre-Paleozoic faults reactivated time and again, propagating into the sedimentary cover (Boyce & Morris, 2002). Boyd and Morris (2002) used comparisons between basement aeromagnetic lineament maps and surface fracture models to identify fault reactivation. Landsat images and spatial distributions of earthquakes were used to identify reactivation of strike-slip faults in basement structures in the Zagros fold and thrust belt that

subsequently influenced sediment deposition and shallow deformations (Hessami et al., 2001; Burberry, 2015). These influences identified by Hessami et al. (2001) included facies constraints, sediment thicknesses and trends of fold axes (direct influences on salt tectonics, seismicity, and hydrocarbon productivity of a fold-thrust system). Burberry et al. (2011) have shown that reactivation of offshore basement faults in the Zagros and Makran area has led to a variety of subsequent structures (salt diapirism and associated folding) in the subsurface.

Although experimental analog methods have been applied to the study of basement structures and effects on subsequent fault reactivation have been undertaken, these efforts have emphasized normal faulting situations with much less work done on reverse or strike-slip terrains. In Burberry and Swiatlowski (2016), similar models were run replicating the Dinaric Alps. The analog models in that study examined pre-existing basement faults extending to various depths into the surface layers, and at much greater oblique angles to transport. This case study builds on that previous work (Burberry and Swiatlowski, 2016); it is also confined to the pre-existing basement faults and examines *en echelon* faults that are at a lesser degree of obliquity to transport. The Burberry and Swiatlowski (2016) study also found that oblique basement-confined faults tended to be reactivated as strike-slip faults, in agreement with this study. Clay modeling (Miller & Mitra, 2011) has been used to examine the resulting secondary faulting in a trishear zone above pre-existing normal, reverse, and vertical basement faults perpendicular to transport direction. Their tests showed that there were numerous characteristic features, such as fault propagation folds, that could be tracked in both experimental models and

natural occurrences. Higgins and Harris (1997) were able to successfully portray basement fault reactivation potentials in extensional systems using sandbox modeling. Their main focus was how surface deformations differed when surface layer compositions were changed. They concluded that faulting in a surface system without a basal ductile layer was more likely to be influenced by reactivated basement faults.

The Sawtooth Range is an ideal location to study basement structure influences on fault reactivation. Multiple faults have reactivated and deactivated, yet the overall structure has remained well-preserved (Fuentes et al., 2012). The underlying basement structures are likely to be influenced by the Great Falls Tectonic Zone; a 1.8 Ga northeast-trending zone (Boerner et al., 1998). Atop this zone lie multiple imbricate thrusts and asymmetric folds (Holl & Anastasio, 1992). The variation in orientation and thrust spacing of these structures indicates fault reactivation influenced by prominent, varying basement structures (Hardebol et al., 2007). This basement-surface relationship in the Sawtooth Range has received limited previous attention, especially with respect to modeling. The case study will help answer questions about the region that have been long left unanswered and have future applications to other fold-thrust systems, as well as provide new insight into *en echelon* basement fault reactivation. These questions include: What is the full story behind the development of the Sawtooth Range? What is the full extent of hydrocarbon plays? When is the next earthquake in the region likely to occur? It can also lead to the potential prediction of major earthquakes along other known or unknown basement faults, such as the 6.6 Richter scale earthquake in Bam, Iran, in 2003, or the 5.6 Richter scale earthquake in Virginia, USA, in 2011. Both

earthquakes occurred along reactivated basement faults, and both proved quite destructive.

This project's goal is to develop an understanding of the relationship of such pre-existing basement structures and their influence on subsequent fault reactivation and deformation. In order to help achieve our goals we have developed a map indicating notable regions of surface deformation structures and trends. Second, field data indicating stress directions and relationships were collected to verify deformation movements in the surface structures in the area. Third, a map of notable basement structural trends was created using geophysical data, seismic data, and well logs to determine the location of potentially reactivated faults. Fourth, we have turned to analog sandbox models to obtain a better understanding of the Sawtooth Range deformation development. In Maillot & Koyi (2006), it was demonstrated that varying pre-existing conditions in a sandbox model caused variations in subsequent thrust system geometries, and were able to prove their dissipation theory to within 3°. This research intends to use sandbox models to analyze the potential for fault reactivation in situations nearly analogous to the Sawtooth Range. Lastly, the resulting maps and images (from stages 1 and 2 and 3), and models (from stage 4), were compared to assess how well the model scenarios represented the development of the Sawtooth Range. These items were then used to assess basement fault reactivation, its effects on subsequent surface deformations, potential seismic risk, and hydrocarbon productivity.

GEOLOGIC SETTING OF THE STUDY AREA

The Sawtooth Range, in northwestern Montana (USA), is located at the foreland of the Lewis Thrust System (Fuentes et al., 2012); a thrust system that compromises the El Dorado, the Lewis, and the Hoadley Thrusts (Figure 1a; Fuentes et al., 2012). The general trend of the Sawtooth Range is slightly west of north to slightly east of south, plunging to the north and portraying an arcuate shape with the apex to the northeast. The Augusta Syncline lies to the east. Narrowing in on the study area (Figure 1b), our particular focus was on the sheets exposed along the Gibson Reservoir, following the Range south to the region where the trend of the Range takes a sharp turn and runs slightly north of west to slightly south of east.

The tectonic history of the Sawtooth Range begins in the late Archean to early Proterozoic. Two cratons in the North American Cordillera, the Medicine Hat, metasedimentary rocks ranging from 2.6 to 3.3 Ga and the Wyoming Craton, with metasedimentary rocks ranging from 2.5 to 3.5 Ga, began colliding in the Paleoproterozoic (Foster et al., 2006). The resulting deformation zone is known as the Great Falls Tectonic Zone (GFTZ) and was active approximately 1.77-1.86 Ga (Foster et al., 2006). These zones can be seen in Figure 2. The GFTZ contains subduction-related igneous rocks indicative of the closure of an ocean basin and a potential suture between the two Archean cratons (Mueller et al., 2002). The rock chemistry indicates that the collisions resulted in dual subduction zones, with the Medicine Hat block over-riding the GFTZ, and the GFTZ over-riding the Wyoming Craton (Holm & Schneider, 2002). This

zone may have also been reactivated as a Paleoproterozoic NE-SW trending shear zone as indicated by electromagnetic field anomalies (Boerner et al., 1998). In the previously mentioned study, the electromagnetic response of the GFTZ is seen as weak and dissimilar to other exposed Paleoproterozoic orogens. After the deformation slowed, the area went into a rather long period of tectonic quiescence, with primary deposition coming from shallow marine deposits, first from the Panthalassic Ocean and later the Cretaceous Interior Seaway (Fuentes et al., 2012). The rocks of this period compose the majority of the thrust sheets involved in the Sawtooth Range (Figure 3). We will mention the Cambrian succession here as it is present in the region, most notably at Cataract Falls. This succession begins with an unconformity and the Flathead Sandstone, ends with the unconformity at the Devil's Glen Dolomite, and is made up of various limestones in between. The Devonian-aged Three Forks Formation is represented in this region by shales and mudstones. This is overlain by the Mississippian Madison Group, divided into the Allen Mountain Limestone, composed of gray limestones characterized by fossils and chert nodules, and the overlying Castle Reef Dolomite, composed of a light gray, generally crystalline dolomite. Getting into the Jurassic, we encounter the Ellis group, composed of primarily sandstones mixed with shales and the occasional presence of glauconite. And, for this study's sake, we end with the Jurassic-aged Morrison Formation, a marker layer characterized by reddish-orange shales and sandstones. (Mudge, 1972; Fuentes et al., 2012)

Tectonic activity resumed in the late Jurassic when the Interior Seaway regressed and the deformations that resulted in the current topography of the Sawtooth Range

occurred. Western uplift in the region began in the late Jurassic with the onset of the Sevier Orogeny (Mudge, 1970; Mudge, 1972). Uplift increased in the late Cretaceous with a renewed pulse from the Laramide Orogeny into the Paleocene and Eocene (Mudge, 1970; Mudge, 1972; Fuentes et al., 2012). A theory is that the numerous faults were in fact a result of differing initial tapers in the hanging wall block, much more subsidence had occurred in the west, and internal strength (Fuentes et al., 2012). The tectonic subsidence towards the west resulted in a greater initial basement taper resulting in thicker, stronger formations. This differs from the lower initial basement taper and thinner, weaker formations in the eastern Sawtooth Range. The combination of this tectonic subsidence and the growing flexure to the east, resulted in deep large-scale sheets in the west and the shallow, steeply stacked, imbricate thrusts in the eastern Sawtooth Range (Figure 4) (Boyer, 1995; Fuentes et al., 2012). Deformation resulted in numerous NW-SE trending fault systems, including the Hoadley Thrust, Lewis Thrust, and El Dorado Thrust Zones. Originally, the primary deformation of the Sevier Orogeny came from the collision of the Farallon plate with the North American plate, and the resulting island arc accretion. This deformation style was thin-skinned without involving basement rock. Later the flat-slab subduction of the oceanic crust of the Farallon plate, caused the wedge that produced the basement-involved Laramide Orogeny. However, there was lithospheric tearing in the slab, resulting in the Sawtooth Range experiencing Sevier-style deformation during what is conventionally known as “Laramide” time. It has also been presented by Copeland et al. (2017) that deformation during the Laramide was locally variable, and that much of the uplift in the northern Rockies can be attributed

to the encroachment of a broad "Nevadaplano" plateau. Presently, the Sawtooth Range is potentially experiencing orogenic collapse due to a northern shift in Pacific plate movement, and is indicated by the late-developing normal faults to the west in Figure 4 (Fuentes et al., 2012).

METHODS

REMOTE SENSING INTERPRETATIONS

Initial assessment began with an analysis of remotely sensed data. Aerial photographs, topographic maps, and Landsat images obtained from the UGSS archives (USGS.gov, 2015) were used to establish a photomosaic of the regional area. Established fault data (USGS.gov, 2015) were overlain on the photomosaic using ArcGIS (v 10.4). The resulting map was then used to locate surface deformations and pinpoint ideal sites for field data collection. Basement structural trends were developed using aeromagnetic potential data and isostatic residual gravity data (Figures 5, 6; Mankinen et al., 2004), also through the use of ArcGIS. A comparison of these trends with the surface structural map, cross-section data (Mudge, 1970; Mudge, 1972; Holl & Anastasio, 1992; Fuentes et al., 2012), and the results of the field data collection, has demonstrated areas of surface-basement deformation interaction. The interaction of various plausible basement configurations with surface structures has been analyzed with analog models, and

displayed a growing complexity of surface deformation as more faults were added to the basement.

FIELD DATA COLLECTION

The field data collected were collected in the Sawtooth Range, Montana (Figures 7 & 8). Study sites included the Gibson Reservoir, Benchmark Road, Cataract Falls, etc. Data collected included bedding plane orientations (right-hand rule (RHR) strike-dip, meaning dip is always to the right of given strike orientation), fracture orientations, fold limb orientations, fault locations, including their orientations and movement indications, and sketches and photographs, measured using a standard Brunton compass. This was done over a period of 12 days with a field assistant.

ANALOG SANDBOX MODELS

In this study, a sandbox model has been set up to replicate the behavior of a brittle sand-pack (Figure 8; Burberry, 2015). This consists of a wooden and glass box with one moving wall driven by a stepper motor, and three fixed walls. Two cameras were set up and fixed level to photograph the changes in the top surface of the model as well as the side view (Figure 8a). The modeling box interior is approximately 48 cm wide and in these experiments had initial starting lengths between 591 mm and 670 mm (Table 1). The base, moving wall and fixed wall are made of waterproofed plywood with glass paneling inlayed in the side walls. This causes the model to have a relatively high basal friction. Side walls were left unlubricated, as the model box is wide enough to produce

relatively uncompromised results in the center of the apparatus which are free from edge effects. Typically, representative sections are sliced between 8 and 40 cm from one side wall, removing the 8 cm sections that were affected by edge effects, and leaving 32 cm that can be reasonably used for analysis (Figure 8b). The stepper motor driving the moving wall is capable of doing so at a constant rate of between 4 and 16 mm/hr. Typical model runs use a driving rate of 8 mm/hr. The box is allowed to dry out between experiments, thoroughly cleaned, and freshly sifted sand is used to re-setup each test run.

In this experiment, five analog models were run to investigate the influence variations in pre-existing basement faults had on the surface structures of a subsequently deforming thrust system. Each model consisted of four 5 mm thick "surface" layers of fine-grained quartz sand overlying a 10 mm thick "basement" layer of coarse-grained quartz, poured into the deformation apparatus and smoothed using a scraper, but not compacted (Figure 8c). The sand is sifted before use, to separate the grain size fractions. A standard test sieve (#35) is used, thus the material used in surface layers has a grain size of less than 0.5 mm and the basement layer a grain size of more than 0.5 mm. Marker layers made of dyed fine-grained quartz sand were used to separate the layers. The variables in the setup of the models included the initial starting lengths, basement fault cuts, and the basement layer of the control model. The only along-strike variation introduced in this investigation was a change in the basement fault configuration, and confined only to the basement layer (Figure 8d). These changes were vertical cuts made via a knife blade. The surface layers were undisturbed. Model 1 was a control model and its setup was left undisturbed. Model 2 had a single central fault cut into the

basement layer perpendicular to the moving wall. Model 3 had a single central fault cut into the basement layer slightly oblique to the moving wall. Model 4 had two centered, parallel faults cut into the basement layer slightly oblique to the moving wall. Model 5 had three centered *en echelon* faults cut into the basement layer slightly oblique to the moving mall. Models 1-5 were then shortened to a target bulk shortening of ~15%, with all four models finishing within ~0.756% (Table 1).

In order to allow us to recreate plausible simulations of naturally occurring scenarios, analog models need to be geometrically and dynamically scaled to their prototype. A length ratio of 1.15×10^{-5} is used in these models, which means 5 mm in the model is representative of 435 m in nature. This ratio was specifically chosen to allow the Devonian Colorado Group sedimentary sequence in the Sawtooth Range, which averages 1740 m thick, to be represented by a sand pack 20 mm thick. As the thickness of the Belt Supergroup below the Sawtooth Range is not definitively known, we assumed our "basement" layer in the models to be made up of the Cambrian units (averaging 385 m thickness) and an arbitrary 565 m of Precambrian rocks.

A set of similar dimensionless ratios have been used to correlate the physical properties of the natural and analog materials to allow for dynamic similarity. We must use a coefficient of internal friction that is equal to or close to the value of the rock being simulated. The coefficient of internal friction of the cover sequence is taken to be 0.53-0.64 (Schellart, 2000). In contrast, the coefficient of internal friction of the loose sand used in the models is measured as 0.59 (fine sand) and 0.73 (coarse sand), using shear

and normal stress measurements within the laboratory (Hubbert, 1937; Koyi & Petersen, 1993; Weijermars et al., 1993; Maillot & Koyi, 2006). A ratio that indicates dynamic similarity is the ratio of cohesion to density (Schreurs et al., 2006). In these experiments, for the cover rocks, $C_n/\rho_n = 3.37 \times 10^{-2}$ and $C_m/\rho_m = 1.06 \times 10^{-7}$. The basement units have ratios in nature and the model of 3.37×10^{-2} and 1.24×10^{-7} respectively. Dynamic similarity is achieved by keeping the ratio between values for model and nature similar, in both the cover and the basement layers. The ratio obtained for the cover is 4.44×10^{-6} and for the basement is 3.68×10^{-6}, indicating that dynamic similarity can be assumed to be achieved. These ratios are summarized in Table 2.

During shortening, photographs were taken of the top surface and side view of each model. Photographs were taken every 60 minutes as well as of the initial and final configurations. Side view photographs were used in conjunction with the top surface photographs to track the appearance of new thrust sheets. Top surface photographs, showing the developing wedge and variable fault configurations, were used to compare the models. These photographs were then used to analyze the development of the surface thrust geometries, with emphasis on variations along strike, and the locations of the pre-existing basement fault(s).

Once each model had been shortened close to the desired amount (Table 1) a sand pack was added to preserve the topography and the model was wetted and sliced into cross-sections. Photographs were taken of every cross-section. Representative cross-sections of each model were selected, digitized and analyzed using CorelDraw (v. X7).

These representations were determined based on variations in thrust geometry, orientation, stacking pattern, and quantity within the wedge, as well as the locations of the pre-existing basement fault(s). Volume loss by sand escape is negligible in these models, as the moving wall is a snug fit to both the base and sides of the shortening apparatus.

RESULTS

REMOTE SENSING

The aerial photo (Figure 7) of the region has fault geometries interpreted onto the image. Faults in the NW part of the image trend N-S, and are closely spaced imbricate thrusts. The northwestern corner faults trend north-south and are closely spaced imbricate thrusts, although more fragmented than the other regions. There is an abrupt change to a northwest-southeast fault trend approaching the central-western portion. In the central-western portion, the imbricate thrusts are spaced far apart, with a trend of NW-SE, and continue through the southwestern portion. The central-northern portion faults trend N-S, are evenly spaced imbricate thrusts, and change to a NW-SE trend approaching the central portion of the image. The faults in the central portion trend NW-SE, are closely spaced imbricate thrusts broken up by tuning-fork faults. The central-southern portion has two fault orientations, one imbricate thrust system trending NW-SE, and the other an oblique system trending NE-SW. Faulting here is segmented and spaced further apart.

The eastern portions show a wider, shallower fault spacing indicative of foreland deformation.

The initial remote sensing analysis demonstrated three regions of differing surface deformation. A northern region (Zone 1) is located along the Gibson Reservoir, where the primary structures are the imbricate thrust sheets with an approximate N-S trend. A middle region (Zone 2) is located along Benchmark Road, where the primary structures in the thrusts sheets change orientation to a northwest by southeast trend and geometries appear more convoluted. The final southern region (Zone 3) is located along Elk Creek Road, and is marked by a return in the primary structures' trend to that of one similar to Zone 1. Access to each region was determined via field reconnaissance, public land, and seasonal openings as per Forest Services.

The basement data (Figure 9) consist of iso-residual gravity and magnetic potential maps taken from Mankinen et al. (2004). The intermediate wave iso-residual gravity map (Figure 5) shows a NE-SW trending zone, which Mankinen et al. (2004) has identified as the Great Falls Tectonic zone, located directly beneath the study area. The magnetic potential map (Figure 6) also shows a zone with a NE-SW trend located directly beneath the study area, also most likely the Great Falls Tectonic Zone. These zones will be represented by variable basement cuts in the analog sandbox models covered later.

FIELD DATA

As stated in the previous section, there were three zones investigated in the field. Field data results are as indicated in Table 3 and stereonet Figures 10.1-10.6. Zone 1 includes the region located along the Gibson Reservoir, primarily accessed by footpath, and the eastern portion of the Sun River Canyon, accessed via road cuts along the Sun Canyon Road. Zone 1, also referred to as the Reservoir Zone, is broken down into nine primary thrust sheets, numbered 1-I to 9-A traveling west to east. The thrust sheets were identified by repetitions of Devonian shale and Mississippian carbonate in the succession. Zone 2 includes road cut sites along Benchmark Road and Double Falls, accessed via footpath. For simplicity, the data collection sites in Zone 2 have been amalgamated into the Middle Zone. Zone 3 is the southern region, which includes road cuts along Elk Creek Road and Cataract Falls, accessed via footpath. For simplicity, the data collection sites in Zone 3 have been amalgamated into the South Zone. Bedding plane orientations were observed using the right-hand rule (RHR); dip is always to the right of the used orientation. Fracture data in this section have been left un-rotated. Strike of bedding planes and fractures are given by one end only unless explicitly stated otherwise.

ZONE 1 – RESERVOIR (Figures 10.1 & 10.2)

Thrust Sheet 1-I bedding planes showed a calculated average strike of 179.5° and an average western dip of 47.5°. The rose diagram indicates the primary bedding plane strike bearing 175.5°, with 55.56% occurring between 171° and 180°. The poles of the bedding planes showed a Fisher mean vector plunging 42.6° to 089.5°. The primary

orientation for fractures, as indicated by the rose diagram, has a strike direction of 165.5°, with 27.27% occurring between 161° and 170°. Two secondary orientations show strike directions of 089° and 135°.

Thrust Sheet 2-H bedding planes showed a calculated average strike of 178.73° and an average western dip of 48.82°. The rose diagram indicates the primary bedding plane strike bearing 185.5°, with 54.55% occurring between 181° and 190°. The poles of the bedding planes showed a Fisher mean vector plunging 41.3° to 088.4°. The primary orientation for fractures, as indicated by the rose diagram, has a strike direction of 205.5°, with 27.27% occurring between 201° and 210°. Two significant secondary orientations are strike directions of 215° and 235°. Another minor secondary orientation is a strike direction of 225°.

Thrust Sheet 3-G bedding planes showed a calculated average strike of 173° and an average western dip of 50.1°. The rose diagram indicates the primary bedding plane strike bearing 175.5°, with 100% occurring between 171° and 180°. The poles of the bedding planes showed a Fisher mean vector plunging 39.9° to 083.1°. The fracture data for Sheet 3-G were sparse at our field site and as such will be skewed. There are two primary orientations for fractures, as indicated by the rose diagram, strike directions of 100° and 342°.

Thrust Sheet 4-F bedding planes showed a calculated average strike of 174.44° and an average western dip of 70.33°. The rose diagram indicates the primary bedding plane strike bearing 175.5°, with 66.67% occurring between 171° and 180°. The poles of

the bedding planes showed a Fisher mean vector plunging 19.8° to 084.4°. The primary orientation for fractures, as indicated by the rose diagram, is a strike direction of 085.5°, with 17.24% occurring between 081° and 090°. A secondary orientation for fractures is a strike direction of 105°.

Thrust Sheet 5-E bedding planes showed a calculated average strike of 168° and an average western dip of 63.64°. The rose diagram indicates the primary bedding plane strike bearing 165.5°, with 42.86% occurring between 161° and 170°. The poles of the bedding planes showed a Fisher mean vector plunging 26.5° to 077.9°. The primary orientation for fractures, as indicated by the rose diagram, is a strike direction of 105.5°, with 13.27% occurring between 101° and 110°. Two secondary orientations for fractures are strike directions of 085° and 114°.

Thrust Sheet 6-D bedding planes showed a calculated average strike of 174.83° and an average western dip of 59.42°. The rose diagram indicates the primary bedding plane strike bearing 175.5°, with 83.33% occurring between 171° and 180°. The poles of the bedding planes showed a Fisher mean vector plunging 30.6° to 084.9°. The primary orientation for fractures, as indicated by the rose diagram, is a strike direction of 115.5°, with 26.67% occurring between 111° and 120°. Three secondary orientations are strike directions of 105°, 167°, and 224°.

Thrust Sheet 7-C bedding planes showed a calculated average strike of 175.13° and an average western dip of 57.63°. The rose diagram indicates the primary bedding plane strike bearing 175.5°, with 87.5% occurring between 171° and 180°. The poles of

the bedding planes showed a Fisher mean vector plunging 32.4° to 085.1°. The primary orientation for fractures, as indicated by the rose diagram, is a strike direction of 125.5°, with 57.14% occurring between 121° and 130°.

Thrust Sheet 8-B bedding planes showed a calculated average strike of 181.69° and an average western dip of 48.54°. The rose diagram indicates the primary bedding plane strike bearing 185.5°, with 38.46% occurring between 181° and 190°. The poles of the bedding planes showed a Fisher mean vector plunging 42.2° to 091.6°. The primary orientation for fractures, as indicated by the rose diagram, is a strike direction of 005.5°, with 38.89% occurring between 001° and 010°. A secondary orientation for fractures is a strike direction of 095°.

Thrust Sheet 9-A bedding planes showed a calculated average strike of 177.5° and an average western dip of 30.83°. The rose diagram indicates the primary bedding plane strike bearing 175.5°, with 50.0% occurring between 171° and 180°. The poles of the bedding planes showed a Fisher mean vector plunging 59.3° to 087.5°. The primary orientation for fractures, as indicated by the rose diagram, is a strike direction of 175.5°, with 62.5% occurring between 171° and 180°.

ZONE 2 – MIDDLE (Figures 10.3 & 10.4)

Due to lack of significant outcrops, Zone 2 data have been consolidated into a single Middle Zone. Middle bedding showed a calculated primary average strike of 133.4°, averaging a southwestern dip of 49.75°, and a secondary average strike of 327.0°,

averaging a northeastern dip of 76.33°. The rose diagram indicates the primary bedding plane strike direction of 145.5°, with 30.91% occurring between 141° and 150°. The poles of the bedding planes showed a Fisher mean vector plunging 44.6° to 047.0°. The primary orientation for fractures, as indicated by the rose diagram, is a strike direction of 035.5°, with 12.2% occurring between 031° and 040°. Two significant secondary orientations are strike directions of 216° and 324°, and two minor secondary orientations are strike directions of 075°, and 233°.

ZONE 3 – SOUTH (Figures 10.5 & 10.6)

Due to lack of significant outcrops, Zone 3 data have been consolidated into a single South Zone. South bedding showed a calculated average strike of 139.84° and an average southwestern dip of 35°. The rose diagram indicates the primary bedding plane strike direction of 135.5°, with 23.08% occurring between 131° and 140°. The poles of the bedding planes showed a Fisher mean vector plunging 56.1° to 050.4°. The primary orientation for fractures, as indicated by the rose diagram, is a strike direction of 065.5°, with 18.75% occurring between 061° and 070°. A secondary orientation for fractures is a strike direction of 335°.

ANALOG SANDBOX MODELS

MODEL 1 – Control (UNLDRG 100814)

Model 1 (Figure 11) was set up with no fault cut into the basement layer. The initial starting length was 591 mm and was compressed to a finishing length of 502 mm,

a total base shortening of 15.06%. Total volume loss was 27 mL. Top view photos (Figures 11a & 11b) indicate that faulting propagated roughly even across the surface. Faulting was fairly uniform with similar spacing and geometry throughout. Side view photos (Figure 11c) also indicate a stacked thrust system with fairly uniform geometries.

MODEL 2 – Single Fault Perpendicular to Moving Wall (UNLDRG 102414)

Model 2 (Figure 12) was set up with a single fault cut, centered, into the basement layer perpendicular to the moving wall. The initial starting length was 601 mm and was compressed to a finishing length of 514.5 mm, a total base shortening of 14.393%. Total volume loss was 22 mL. Top view photos (Figures 12a & 12b) indicate that faulting began in the center, above the basement fault cut, and propagated to the edges of the model. Faulting was fairly uniform with similar spacing and geometry throughout. Side view photos (Figure 12c) also indicate a stacked thrust system with fairly uniform geometries.

MODEL 3 – Single Fault Oblique to Moving Wall (UNLDRG 110614)

Model 3 (Figure 13) was set up with a single fault cut, centered, into the basement layer oblique to the moving wall. The initial starting length was 655 mm and was compressed to a finishing length of 556 mm, a total base shortening of 15.115%. Total volume loss was 20 mL. Top view photos (Figures 13a & 13b) indicate that faulting began in the center, above the basement fault cut, and propagated to the edges of the model. Faulting was segmented with variable spacing and geometry throughout. A

number of smaller, cross-cutting faults became visible. Side view photos (Figure 13c) also indicate a stacked thrust system with variable geometries. As the cuts moved closer to the fault cut, base sheets had shallow dips and were more pronounced, while sheets in the upper portion of the stack had steeper dips and become tighter.

MODEL 4 – Two Parallel Faults Oblique to Moving Wall (UNLDRG 012015)

Model 4 (Figure 14) was set up with two parallel faults cut, centered, into the basement layer oblique to the moving wall. The initial starting length was 670 mm and was compressed to a finishing length of 568.5 mm, a total base shortening of 15.149%. Total volume loss was 21 mL. Top view photos (Figures 14a & 14b) indicate that faulting began above the basement fault cuts, and propagated to the edges of the model. Faulting was segmented with variable spacing and geometry throughout. The most significant segments occurred above or between the basement fault cuts. Side view photos (Figure 14c) also indicate a stacked thrust system with variable geometries. Sheets near the right basement fault cut are more pronounced, with a fairly uniform geometry and spacing, as well as steeper dips. Sheets in between the two basement fault cuts are more numerous with shallower dips at the base. Sheets near the left basement fault cut are more numerous with tighter spacing moving up the system, and steeper dips.

MODEL 5 – Three Parallel *En Echelon* Faults Oblique to Moving Wall (UNLDRG 050815)

Model 5 (Figure 15) was set up with three parallel *en echelon* faults cut, centered, into the basement layer oblique to the moving wall. Fault cut distance from the moving wall increased from left to right. The initial starting length was 655 mm and was compressed to a finishing length of 556.5 mm, a total base shortening of 15.038%. Total volume loss was 22 mL. Top view photos (Figures 15a & 15b) indicate that faulting began near the left basement fault cut and propagated towards the right. Faulting was segmented with variable spacing and geometry throughout. The most significant segmenting and changes in direction occurred above the center basement fault cut. Side view photos (Figure 15c) also indicate a stacked thrust system with variable geometries. Sheets near the right basement fault cut are more pronounced with a fairly uniform spacing and geometry and a shallow dip. Sheets near the center basement fault cut have a steeper dip with greater variance in the upper sheets. Sheets near the left basement fault cut are shallower dipping in the base sheets than the upper sheets.

INTERPRETATIONS

REMOTE SENSING

The aerial photos and topographic maps indicate variations in surface fault trend traveling from north to south in the study area. This trend in Zone 1 of N-S changes to

NW-SE in Zone 2, and reverts back to N-S in Zone 3. The surface geometries in Zone 2 become more complex, with branching "tuning fork" faults. This change in surface fault trend and geometries may be explained by the presence of a basement fault trending near perpendicular to bedding and thrust strike orientation. Basement faults perpendicular to transport direction increase horizontal resistance to wedge growth. A fault with a slight obliquity to transport direction would locally increase resistance to wedge growth and allow for fluctuation (along-strike) in that resistance, causing visible changes to orientation of the primary thrust trend. The Scapegoat-Bannatyne Trend, within the GFTZ, is known to have a trend of NE-SW, and placing an arm of the complex under Zone 2 allows for the observed changes. Potential basement fault placements have been marked on Figure 16, as well as the boundaries of Zones 1-3. An examination of the intermediate wave iso-residual gravity map and the magnetic potential map displays a definite strong basement fault trend of NE-SW located directly beneath the Sawtooth Range. This correlates with Mankinen et al. (2004) that this is the expression of the Great Falls Tectonic Zone (Figure 5, 6); however, the resolution of these maps is not enough to distinguish individual faults.

FIELD DATA

In Sheet 1-I, the majority of fractures were syn-folding as there were tighter clusters in the poles plot and rose diagram when left un-rotated (rotated data can be seen in Figure 10.2). The primary fracture strike orientation (165.5°) was approximately parallel to primary bedding strike orientation (175.5°, ~10° difference), while a secondary

fracture strike orientation (089°) was approximately perpendicular (~86.5° difference, dip-parallel).

In Sheet 2-H, the majority of fractures were syn-folding as the clusters were relatively unchanged between the un-rotated and the rotated values (rotated data can be seen in Figure 10.2). The primary fracture strike orientation (205.5°) was approximately parallel to primary bedding strike orientation (185.5°, ~20° difference). The secondary fracture strike orientations of 215° and 225° were approximately strike-parallel (~30° and ~40° differences), and may be potentially basement related. Orientation 235° was in between strike and dip parallel (~50° difference) and is most likely reflective of basement influence.

In Sheet 3-G, there were not enough data to make a firm conclusion as only 2 fractures were measured (rotated data can be seen in Figure 10.2). Both fracture strike orientations, 100° and 342°, were approximately perpendicular to bedding strike orientation (175.5°, ~75.5° and 166.5° differences).

In Sheet 4-F, the majority of fractures were pre-folding as there were tighter clusters in the fractures, poles plot and rose diagram when rotated back to the horizontal (rotated data can be seen in Figure 10.2). The primary fracture strike orientation (085.5°) was approximately perpendicular to primary bedding strike orientation (175.5°, ~90° difference). The secondary strike orientation (105°) was also approximately dip-parallel as well (~70.5° difference).

In Sheet 5-E, the majority of fractures were syn-folding as there were tighter clusters in the poles plot and rose diagram when left un-rotated (rotated data can be seen in Figure 10.2). The primary fracture strike orientation (105.5°) was in between parallel and perpendicular to primary bedding strike orientation (165.5°, ~60° difference), and is reflective of basement influence. The secondary fracture orientations (085° and 114°) were also approximately dip-parallel (~80.5° and ~51.5° differences), with 114° most likely reflective of basement influence.

In Sheet 6-D, the majority of fractures were syn-folding as there were tighter clusters in the poles plot and rose diagram when left un-rotated (rotated data can be seen in Figure 10.2). The primary fracture strike orientation (115.5°) was approximately in between parallel and perpendicular to primary bedding strike orientation (175.5°, ~60° difference), and is most likely reflective of basement influence. The secondary fracture strike orientation of 105° was approximately dip-parallel (~70.5° difference), 167° was approximately strike-parallel (~8.5° difference), and 224° was in between strike and dip-parallel (~48.5° difference), and most likely reflective of basement influence.

In Sheet 7-C, the majority of fractures were syn-folding as there were tighter clusters in the poles plot and rose diagram when left un-rotated (rotated data can be seen in Figure 10.2). The primary fracture strike orientation (125.5°) was approximately in between strike and dip-parallel (~50° difference), and is reflective of basement influence.

In Sheet 8-B, the majority of fractures were pre-folding as there were tighter clusters in the fractures, poles plot and rose diagram when rotated back to the horizontal (rotated data can be seen in Figure 10.2). The primary fracture strike orientation (005.5°) was approximately parallel to primary bedding strike orientation (185.5°, ~180° difference). The secondary fracture strike orientation (095°) was approximately dip-parallel (~90.5° difference).

In Sheet 9-A, the majority of fractures were syn-folding as there were tighter clusters in the poles plot and rose diagram when left un-rotated (rotated data can be seen in Figure 10.2). The primary fracture strike orientation (175.5°) was approximately parallel to primary bedding strike orientation (175.5°, ~0° difference).

In Zone 2, the majority of fractures were syn-folding as there were tighter clusters in the poles plot and rose diagram when left un-rotated (rotated data can be seen in Figure 10.4). The primary fracture strike orientation (035.5°) was approximately perpendicular to primary bedding strike orientation (145.5°, ~110° difference). The secondary fracture strike orientations (216° and 324°) were dip-parallel and strike-parallel respectively (~70.5° and ~178.5° differences).

In Zone 3, the majority of fractures were pre-folding as there were tighter clusters in the fractures, poles plot and rose diagram when rotated back to the horizontal (rotated data can be seen in Figure 10.6). The primary fracture strike orientation (065.5°) was approximately perpendicular to primary bedding strike orientation (135.5°, ~70°

difference). The secondary fracture strike orientation (335°) was approximately strike-parallel (~199.5° difference).

The vast majority of recorded fractures were strike-parallel (within 15° of strike/inverse strike orientation) or dip-parallel (within 15° of dip direction). They also occurred syn-folding, and indicate that transport was up-dip. Fracture orientations between strike-parallel and dip-parallel are most likely reflective of basement influence. These directions are not parallel to σ_1 (dip parallel), which is the most favorable fracture orientation. Also, they are not opening mode-stretching fractures caused by a bending in the thrust sheets. Therefore, the only explanation for these fracture orientations is an outside influence, such as a pre-existing feature or a change in σ_1 over time. However, no major change in σ_1 in this region has been demonstrated that would explain these features (Yonkee and Weil, 2015; Copeland et al., 2017). This indicated strong evidence for a NE-SW trending basement structure and provided support for setting up the models in this study.

ANALOG SANDBOX MODELS

In the analog model suite, Model 1 was run as a control. This model had no basement fault cut, and was intended to serve as a comparison point for later models. As mentioned previously, Model 1 exhibited even fault propagation on the surface, ending in an evenly spaced imbricate thrust stack, with little variation in surface trend and

basement dip (Figure 17). Models 2-5 will now be described based on their differences to Model 1.

In Model 2, a single fault perpendicular to the transport direction was cut in the basement layer. This resulted in very distinct propagation differences from Model 1. Propagation on the surface, in Model 2, began in the center of the box and grew toward the edges of the model, whereas in Model 1 propagation was even across the surface. This may be attributed to the basement fault cut creating more resistance to wedge growth, causing earlier onset in brittle deformation, limiting horizontal growth, and increasing vertical growth. The end result was an evenly spaced imbricate thrust stack, indicating that a perpendicular fault cut does little to alter surface fault trend orientation (Figure 18). This is also supported by even fault spacing on the surface and very little change in surface fault system trend.

In Model 3, a single fault oblique to the transport direction was cut in the basement layer. Fault propagation once again began in the center of the box and grew toward the edges of the model, similar to Model 2 and differing from Model 1. This provides more support that the basement fault cuts increase resistance to transport and wedge growth and can be seen in the early increase in vertical growth above the basement fault cut. Surface fault trends were also more segmented above the basement cut during growth, leading to many "tuning forks" in the final result. There is also closer spacing in the imbricate thrust stack nearer to the basement fault cut, as seen in the cross sections of Figure 19.

In Model 4, two faults oblique to the transport direction were cut in the basement layer. Once again surface propagation begins above the basement fault cuts and grew toward the edges of the model, similar to Models 2 and 3 and differing from Model 1. The faults increased the resistance to horizontal transport and wedge growth, and caused more segmenting in surface fault trends. The end result was most similar to Model 3. However, the surface trends were even more segmented above the basement fault cuts. There was also faulting oblique to the primary surface trend. The cross-sections displayed the greatest variations along strike in Models 1-4 (Figure 20). The imbricate thrusts near the right basement fault cuts (first fault encountered as cross section cut depth increased), were steeply dipping, and evenly spaced. The thrusts in between the two basement fault cuts were more numerous, shallow dipping and closely spaced, most likely due to an increase in horizontal resistance. The surface faults near the left fault are similar in geometry to the thrust faults between basement cuts, yet steeper dipping. This model is indicative that increasing the number of basement fault cuts increases the variation of complexity and changes in surface fault geometries. These variations are seen mainly in thrust sheet spacing, dip, and surface trend variation.

In Model 5, three *en echelon* faults oblique to transport direction were cut in the basement layer. This model exhibited the greatest differences to Model 1. Propagation in the surface faulting began above the left basement fault cut (the one furthest in cross section cut depth) and grew toward the edges of the model. This growth became more pronounced as the middle and right basement fault cuts became involved, indicating a growing resistance to horizontal transport and wedge growth. Variations in surface trend

and segmentation occurred at or between basement fault cuts. The final surface result of Model 5 is most similar to what is observed in the Sawtooth Range. In viewing the cross sections, the imbricate thrusts near the right and left basement fault cuts are shallower and steeper with greater variation in the upper stack near the center basement fault cut (Figure 21). This model indicates that to achieve variations in surface trend similar to those in the Sawtooth Range, the discrete basement faults forming the Scapegoat-Bannatyne Trend would most likely need to be *en echelon* (Figure 16).

DISCUSSION

The aerial photo analysis demonstrated that the Sawtooth Range is fragmented with various changes in fault trend direction. This indicates another contributing factor outside the realm of collision-related transport, most likely basement influenced. The fault geometries must have been influenced by significant basement fault reactivation. The most likely source is the Great Falls Tectonic Zone, as indicated by the study of the basement lineations, magnetic potential and residual gravity maps. Taking this into account, analog sandbox models were run to simulate various potential basement fault configurations.

The models used in this project sufficiently satisfied the dynamic similarity constraints for plausibility. This allowed us to make direct comparisons between the natural deformations in the Sawtooth Range and the deformation in the analog sandbox

models. The sandbox models demonstrated that a significant *en echelon* basement fault zone (such as the strands of the Scapegoat Bannatyne trend) is needed to produce the variable surface deformations seen in the Sawtooth Range.

While the models generated in this project sufficiently satisfied the dynamic similarity constraints, there are still a few factors that could be altered to provide an even more accurate comparison. This project assumed that the entire basement was made up of rock with equal thicknesses, densities, friction, and cohesion throughout. However, it would be reasonable to assume that these factors would be different within the basement fault zone (GFTZ) than outside of the fault zone. It would also be reasonable to assume pre-existing displacement would be seen in the basement fault zone, which could influence subsequent deformation development in both the basement and surface layers. Models tailoring to these discrepancies would provide even more accurate results.

The significance lies in the potential applications of this case study. The study is being performed specifically in the Sawtooth Range; yet, the final intention is to generate a model to apply to other fold-thrust belts across the world. The model will indicate potential movements in a complex basement system with strong influences on the associated cover system. It would be a means of determining the seismic risk of the belt. This is useful in its application to intracontinental fault systems as some of the strongest, most-damaging earthquakes occur along them (Talwani 1999). Prediction of seismic risk along such systems is of value to public health and safety, especially along zones that are overdue for a large earthquake, such as the New Madrid zone (Cramer 2001). This model

has the potential to help scientists determine where to place advanced warning systems for large-scale, basement oriented, seismic events. The Sawtooth Range can serve to further future research in basement fault reactivation's influence on earthquake potential as there are numerous historical earthquakes centered around the surface deformation and the Great Falls Tectonic Zone (Figure 22).

The secondary benefit of developing this model is that it will allow more accuracy in managing petroleum plays. If fault reactivation and movement are predicted, the hydrocarbon industry is aided in determining hydrocarbon migration in advance. An analysis of the faults can indicate their potential for reactivation, which implies their likelihood as a conduit for hydrocarbons as well as the potential timing of the conduit's activity. It also serves to prevent exploration based on the likelihood of the faults causing immature hydrocarbons to saturate a good play. This aids in determining the timing and location of trap development. Hydrocarbon fields also tend to be common along basement faulting. This is evident in Figure 23, indicating hydrocarbon plays in Montana along the Pendroy Fault, South Arch trend, and an arm of the Scapegoat-Bannatyne trend, all of which are basement faults.

CONCLUSION

The final assessment of this case study of the southern Sawtooth Range, indicates that the surface deformation was significantly altered by a pre-existing basement

deformation in the Great Falls Tectonic Zone, namely the Scapegoat-Bannatyne trend. During the Laramide Orogeny, the surface fold-thrust system dynamics was altered due to basement fault reactivation. Analog sandbox models were developed and tested to analyze the potential basement fault configurations. It was determined that in order to achieve the fluctuation in fault geometries observed in the southern Sawtooth Range, the basement faulting must be *en echelon* and oblique to the transport direction. Surface data measurements and observations confirmed that while most fracture orientations and bedding planes were indicative of strike-parallel and dip-parallel formation, there were numerous pronounced intermediate orientations. Since no significant changes to σ_1 have occurred, these measurements indicated a NE-SW trend that can only be explained by the basement Scapegoat-Bannatyne trend, a part of the Great Falls Tectonic Zone. These findings are in agreement with the analog models. Future research will find application in seismic hazard and hydrocarbon pool assessment.

REFERENCES

Ahmadhadi, F., Lacombe, O., and Daniel, J., 2007, Early reactivation of basement faults in central Zagros (SW Iran); evidence from pre-folding fracture patterns in Asmari Formation and lower Tertiary paleogeography Frontiers in earth science, *in* Springer, p. 205-228.

Aktepe, S., Marfurt, K.J., and Perez, R., 2008, Attribute expression of basement faulting; time versus depth migration: Leading Edge [Tulsa, OK], v. 27, p. 360-367, doi: 10.1190/1.2896627.

Al-Ameri, T., 2014, Oil biomarkers, isotopes, and palynofacies are used for petroleum system type and migration pathway assessments of Iraqi oil fields: Arabian Journal of Geosciences, p. 1-23, doi: 10.1007/s12517-014-1606-5.

Alpha, A.G., 1955, Tectonic history of north central Montana: p. 129-142.

Anderson, E.M., 2012, The dynamics of faulting: Geological Society Special Publications, v. 367, p. 231-246, doi: 10.1144/SP367.16.

Boerner, D.E., Craven, J.A., Kurtz, R.D., Ross, G.M., and Jones, F.W., 1998, The Great Falls tectonic zone; suture or intracontinental shear zone? Canadian Journal of Earth Sciences = Revue Canadienne Des Sciences De La Terre, v. 35, p. 175-183.

Boyce, J.I., and Morris, W.A., 2002, Basement-controlled faulting of Paleozoic strata in southern Ontario, Canada; new evidence from geophysical lineament mapping: Tectonophysics, v. 353, p. 151-171.

Boyer, S.E., 1995, Sedimentary basin taper as a factor controlling the geometry and advance of thrust belts: American Journal of Science, v. 295, p. 1220-1254.

Burberry, C.M., and Swiatlowski, J.L., 2016, Evolution of a fold-thrust belt deforming a unit with pre-existing linear asperities: Insights from analog models: Journal of Structural Geology, v. 87, p. 1-18.

Burberry, C.M., and Palu, J.M., 2016, The influence of the Great Falls Tectonic Zone on the thrust sheet geometry of the southern Sawtooth Range, Montana, USA: Geological Magazine, v. 153, p. 845-865.

Burberry, C.M., 2015. The effect of basement fault reactivation on the Triassic-Recent geology of Kurdistan, N Iraq. Journal of Petroleum Geology, v38 (1) p37-58.

Burberry, C.M., Jackson, C.A.L., and Cosgrove, J.W., 2011, Late Cretaceous to Recent deformation related to inherited structures and subsequent compression within the Persian Gulf; a 2D seismic case study: Journal of the Geological Society of London, v. 168, p. 485-498, doi: 10.1144/0016-76492010-022.

Copeland, P., Currie, C.A., Lawton, T.F., and Murphy, M.A., 2017, Location, location, location: The variable lifespan of the Laramide orogeny: Geology, v. 45, p. 223-226, doi: 10.1130/G38810.1.

Cramer, C.H., 2001, A seismic hazard uncertainty analysis for the New Madrid seismic zone: Engineering Geology, v. 62, p. 251-266.

Eisenstadt, G., and De Paor, D.G., 1987, Alternative model of thrust-fault propagation: Geology [Boulder], v. 15, p. 630-633.

Foster, D.A., Mueller, P.A., Mogk, D.W., Wooden, J.L., and Vogl, J.J., 2006, Proterozoic evolution of the western margin of the Wyoming Craton; implications for the tectonic and magmatic evolution of the Northern Rocky Mountains: Canadian Journal of Earth Sciences = Revue Canadienne Des Sciences De La Terre, v. 43, p. 1601-1619, doi: 10.1139/E06-052.

Fuentes, F., DeCelles, P.G., and Constenius, K.N., 2012, Regional structure and kinematic history of the Cordilleran fold-thrust belt in northwestern Montana, USA: Geosphere, v. 8, p. 1104-1128, doi: 10.1130/GES00773.1.

Ghosh, K., and Mitra, S., 2009, Structural controls of fracture orientations, intensity, and connectivity, Teton Anticline, Sawtooth Range, Montana: AAPG Bulletin, v. 93, p. 995-1014, doi: 10.1306/04020908115.

Hafner, W., 1951, Stress distributions and faulting: Geological Society of America Bulletin, v. 62, p. 373-398, doi: 10.1130/0016-7606(1951)62[373:SDAF]2.0.CO;2.

Hardebol, N.J., Callot, J., Faure, J., Bertotti, G., and Roure, F., 2007, Kinematics of the SE Canadian fold-and-thrust belt; implications for the thermal and organic maturation history Frontiers in earth science, *in* Springer, p. 179-202.

Harper, T., Fossen, H., and Hesthammer, J., 2001, Influence of uniform basement extension on faulting in cover sediments: Journal of Structural Geology, v. 23, p. 593-600.

Healy, D., Sibson, R.H., Shipton, Z.K., and Butler, R., 2012, Stress, faulting, fracturing and seismicity; the legacy of Ernest Masson Anderson: Geological Society Special Publications, v. 367, p. 1-6, doi: 10.1144/?SP367.1.

Hengmao, T., and Yin, A., 2011, Reactivation tendency analysis; a theory for predicting the temporal evolution of preexisting weakness under uniform stress state: Tectonophysics, v. 503, p. 195-200, doi: 10.1016/j.tecto.2011.02.012.

Hessami, K., Koyi, H.A., and Talbot, C.J., 2001, The significance of strike-slip faulting in the basement of the Zagros fold and thrust belt: Journal of Petroleum Geology, v. 24, p. 5-28.

Hesthammer, J., and Fossen, H., 2000, Uncertainties associated with fault sealing analysis: Petroleum Geoscience, v. 6, p. 37-45.

Higgins, R.I., and Harris, L.B., 1997, The effect of cover composition on extensional faulting above re-activated basement faults; results from analogue modelling: Journal of Structural Geology, v. 19, p. 89-98.

Holl, J.E., and Anastasio, D.J., 1992, Deformation of a foreland carbonate thrust system, Sawtooth Range, Montana: Geological Society of America Bulletin, v. 104, p. 944-953, doi: 10.1130/0016-7606(1992)104<0944:DOAFCT>2.3.CO;2.

Holm, D., and Schneider, D., 2002, (super 40) Ar/ (super 39) Ar evidence for ca. 1800 Ma tectonothermal activity along the Great Falls tectonic zone, central Montana: Canadian Journal of Earth Sciences = Revue Canadienne Des Sciences De La Terre, v. 39, p. 1719-1728, doi: 10.1139/E02-069.

Hubbert, M.K., 1937, Theory of scale models as applied to the study of geologic structures: Geological Society of America Bulletin, v. 48, p. 1459-1519.

Koyi, H., 1997, Analogue modelling; from a qualitative to a quantitative technique; a historical outline: Journal of Petroleum Geology, v. 20, p. 223-238, doi: 10.1306/BF9AB78D-0EB6-11D7-8643000102C1865D.

Koyi, H. & Petersen, K. 1993. Influence of basement faults on the development of salt structures in the Danish Basin. Marine and Petroleum geology, 10(2) pp82-94.

Krantz, R.W., 1991, Measurements of friction coefficients and cohesion for faulting and fault reactivation in laboratory models using sand and sand mixtures: Tectonophysics, v. 188, p. 203-207.

Leclere, H., and Fabbri, O., 2013, A new three-dimensional method of fault reactivation analysis: Journal of Structural Geology, v. 48, p. 153-161, doi: 10.1016/j.jsg.2012.11.004.

Maillot, B. & Koyi, H. 2006. Thrust dip and thrust refraction in fault-bend folds: analogue models and theoretical predictions. Journal of Structural Geology 28(1), 36-49.

Mankinen, E.A., Hildebrand, T.G., Zientek, M.L., Box, S.E., Bookstrom, A.A., Carlson, M.H., and Larsen, J.C., 2004, Guide to geophysical data for the Northern Rocky

Montana Bureau of Mines and Geology, 2017, http://data.mbmg.mtech.edu/mapper/mapper.asp?view=Quakes& (accessed June 2017)

Mountains and adjacent areas, Idaho, Montana, Washington, Oregon, and Wyoming: U. S. Geological Survey : Reston, VA, United States, .

Miller, J.F., and Mitra, S., 2011, Deformation and secondary faulting associated with basement-involved compressional and extensional structures: AAPG Bulletin, v. 95, p. 675-689, doi: 10.1306/09131010007.

Mohialdeen, I.M., Hakimi, M.H., and Al-Beyati, F.M., 2013, Biomarker characteristics of certain crude oils and the oil-source rock correlation for the Kurdistan oilfields, Northern Iraq: Arabian Journal of Geosciences, p. 1-17.

Mudge, M.R., 1972, Structural geology of the Sun River Canyon and adjacent areas, northwestern Montana: U. S. Geological Survey: Reston, VA, United States, , B1-b52 p.

Mudge, M.R., 1970, Origin of the disturbed belt in northwestern Montana: Geological Society of America Bulletin, v. 81, p. 377-392, doi: 10.1130/0016-7606(1970)81[377:OOTDBI]2.0.CO;2.

Mudge, M.R., Earhart, R.L., Clayton, J.L., Nichols, K.M., Campbell, H.W., and Scott, D.F., 1984, Mineral resource potential and geology of wilderness study area east of the Bob Marshall Wilderness, Teton and Lewis and Clark counties, Montana: U. S. Geological Survey : Reston, VA, United States, .

Mueller, P.A., Heatherington, A.L., Kelly, D.M., Wooden, J.L., and Mogk, D.W., 2002, Paleoproterozoic crust within the Great Falls tectonic zone; implications for the assembly of southern Laurentia: Geology [Boulder], v. 30, p. 127-130.

Qamar, A., Kogan, J., and Stickney, M.C., 1982, Tectonics and recent seismicity near Flathead Lake, Montana: Bulletin of the Seismological Society of America, v. 72, p. 1591-1599.

Schellart, W., 2000. Shear test results for cohesion and friction coefficients for different granular materials: scaling implications for their usage in analogue modelling. Tectonophysics 324 p1-16.

Scholz, C.H., 1989, Mechanics of faulting: Annual Review of Earth and Planetary Sciences, v. 17, p. 309-334.

Talwani, P., 1999, Fault geometry and earthquakes in continental interiors: Tectonophysics, v. 305, p. 371-379.

Weijermars, R. 1992. Progressive deformation in anisotropic rocks. Journal of Structural Geology 14(6) p723-742.

Yonkee, W.A., and Weil, A.B., 2015, Tectonic evolution of the Sevier and Laramide belts within the North American Cordillera orogenic system: Earth-Science Reviews, v. 150, p. 531–593, doi: 10.1016 /j .earscirev .2015 .08 .001.

MULTIMEDIA

TABLES

TABLE 1 – Analog Sandbox Data Models 1-5

MODEL NUMBER	START LENGTH	END LENGTH	BULK SHORTENING	VOLUME LOSS
1. UNLDRG100814	591 mm	502 mm	15.06%	27 mL
2. UNLDRG102414	601 mm	514.5 mm	14.393%	22 mL
3. UNLDRG110614	655 mm	556 mm	15.115%	20 mL
4. UNLDRG012015	670 mm	568.5 mm	15.149%	21 mL
5. UNLDRG050815	655 mm	556.5 mm	15.038%	22 mL

TABLE 2 – Scaling Parameters

QUANTITY	NATURE	MODEL	SCALING RATIO
Acceleration due to gravity (m/s^2)	9.81	9.81	$a_m/a_n = 1$
Thickness – Devonian-Cretaceous units	1740 m	20mm	$L_m/L_n = 1.15 \times 10^{-5}$
Thickness – Cambrian & basement units	950 m	10mm	$L_m/L_n = 1.15 \times 10^{-5}$
Density – cover units ($kg.m^{-3}$)	2440-2580	1740	ρ_m/ρ_n = 0.67-0.71
Density – shale ($kg.m^{-3}$)	2200-2300	1308	ρ_m/ρ_n = 0.56-0.59
Density - basement ($kg.m^{-3}$)	2667	1730	ρ_m/ρ_n = 0.65
Friction coefficient (cover units)	0.53-0.64	0.59	μ_m/μ_n = 0.92-1.11
Friction coefficient (basement)	0.64	0.73	μ_m/μ_n = 1.14
Cohesion (cover units)	60 MPa	185 Pa	$C_m/C_n = 3.08 \times 10^{-5}$
Cohesion (basement)	90 MPa	215 Pa	$C_m/C_n = 6.94 \times 10^{-6}$
Dynamic similarity ratio (avg. cover)	2.39×10^{-2}	1.06×10^{-7}	Ratio m/n = 4.44×10^{-6}
Dynamic similarity ratio (basement)	3.37×10^{-2}	1.24×10^{-7}	Ratio m/n = 3.68×10^{-6}
Shortening rate	0.2 cm/yr	1.75×10^{4} cm/yr	8.75×10^{4}

Burberry & Palu (2016), material properties in nature from Daly et al. (1996) and Schellart (2000)

TABLE 3 - Field Data Zones 1-3

ZONE/SHEET	BEDDING ORIENTATION (RHR S/D)	FRACTURE ORIENTATION (S/D)	FRACTURE ORIENTATION CONTINUED
Zone 1/ Sheet 1-I	177/51.5°	162/18°W	096/55°S
	175/48°	165/20°W	086/66°S
	176/46°	150/30°W	
	184/48°	165/34°W	
	177/53°	136/35°W	
	186/43°	087/71°S	
	181/45°	140/40°W	
	181/48°	093/68°S	
	179/45°	130/70°S	
Zone 1/Sheet 2-H	171/59°	217/66°W	234/41°N
	174/57°	200/44°W	233/51°N
	175/54°	225/37°W	280/42°N
	182/50°	207/45°W	234/56°N
	189/40°	226/55°N	216/70°W
	175/48°	234/60°N	207/38°W
	180/43°	220/54°W	224/55°W
	183/44°	230/53°N	218/45°W
	172/49°	196/55°W	214/54°W
	185/46°	204/55°W	211/46°W
	180/47°	207/43°W	204/50°W
Zone 1/Sheet 3-G	174/44°	100/84°S	
	170/49°	342/72°E	
	175/59°		
	176/55°		
	172/50°		
	170/51°		
	171/46°		
	175/50°		
	173/44°		
	174/53°		
Zone 1/Sheet 4-F	182/74°	297/55°N	130/35°S
	177/76°	256/77°N	086/15°S
	172/80°	075/47°S	145/15°W

	190/62°	102/68°S	170/10°W
	170/70°	103/66°S	160/38°W
	171/66°	105/57°S	086/45°S
	170/60°	175/34°W	095/27°S
	168/74°	084/22°S	106/4°S
	170/71°	244/69°N	123/12°S
		078/7°S	150/31°W
		082/5°S	055/45°S
		229/54°N	152/18°W
		212/45°W	120/19°S
		084/55°S	130/22°S
		100/18°S	
Zone 1/Sheet 5-E	176/73°	236/25°N	067/48°S
	165/50°	100/42°S	100/40°S
	178/64°	072/75°S	088/82°S
	176/70°	116/78°S	095/35°S
	180/54°	120/46°S	101/46°S
	169/66°	283/47°N	090/49°S
	170/54°	252/54°N	070/32°S
	167/65°	074/81°S	093/34°S
	170/69°	094/77°S	076/35°S
	160/64°	064/68°S	085/33°S
	161/65°	182/36°W	347/86°E
	166/60°	251/74°N	083/21°S
	158/70°	115/43°S	095/74°S
	156/67°	061/81°S	070/80°S
		104/31°S	057/47°S
		182/33°W	204/24°W
		109/65°S	040/71°E
		188/25°W	085/85°S
		104/50°S	095/81°S
		115/60°S	093/68°S
		210/43°W	117/78°S
		155/34°W	084/64°S
		155/37°W	105/65°S
		150/36°W	089/72°S
		125/21°S	085/63°S
		135/35°S	081/27°S
		140/24°W	110/58°S
		054/50°S	105/54°S
		239/54°N	138/32°W

		056/30°S	114/53°S
		057/47°S	125/60°S
		225/39°W	283/22°N
		221/34°W	272/19°N
		202/30°W	086/42°S
		195/37°W	074/38°S
		258/37°N	342/51°E
		260/28°N	269/59°N
		256/22°N	104/35°S
		069/74°S	106/36°S
		075/75°S	343/84°E
		079/60°S	102/34°S
		070/30°S	273/89°N
		235/69°N	104/39°S
		230/55°N	140/82°W
		082/55°S	106/37°S
		257/30°N	136/41°W
		259/84°N	116/36°S
		123/42°S	086/65°S
		206/47°W	248/71°N
		216/73°W	122/37°S
		099/80°S	114/39°S
		120/53°S	103/36°S
		238/62°N	115/45°S
		072/72°S	125/39°S
		259/73°N	114/45°S
		280/82°N	100/36°S
		132/53°S	
Zone 1/Sheet 6-D	175/55°	165/54°W	116/66°S
	174/60°	230/24°N	165/35°W
	171/51°	228/29°N	220/31°W
	173/53°	215/33°W	
	181/61°	130/47°S	
	171/58°	109/45°S	
	174/63°	148/25°W	
	171/56°	109/54°S	
	180/67°	120/58°S	
	173/61°	118/59°S	
	176/63°	110/45°S	
	179/65°	111/46°S	

Zone 1/Sheet 7-C	183/59°	125/63°S	
	174/58°	127/75°S	
	172/65°	140/76°W	
	173/56°	125/73°S	
	176/52°	126/70°S	
	179/56°	184/20°W	
	171/58°	213/58°W	
	173/57°		
Zone 1/Sheet 8-B	176/54°	097/87°S	005/77°E
	181/65°	088/81°S	007/76°E
	176/50°	099/82°S	003/67°E
	181/59°	079/43°S	005/57°E
	178/53°	260/73°N	358/74°E
	140/46°	210/46°W	
	183/46°	209/70°W	
	190/44°	199/52°W	
	188/45°	180/53°W	
	194/45°	035/34°E	
	191/41°	004/68°E	
	189/43°	002/81°E	
	195/40°	000/67°E	
Zone 1/Sheet 9-A	180/27°	233/69°N	173/55°W
	174/29°	250/70°N	171/60°W
	173/29°	165/62°W	
	185/36°	175/57°W	
	170/35°	176/52°W	
	183/29°	177/63°W	
Zone 2	135/66°	120/27°S	
	127/56°	030/66°E	
	124/57°	035/60°E	
	135/45°	044/48°E	
	137/51°	071/68°S	
	132/36°	224/84°W	
	130/41°	212/66°W	
	134/40°	222/79°W	
	131/45°	087/68°S	
	134/38°	212/75°W	
	105/20°	050/75°S	
	130/17°	048/71°S	

	133/20°	038/75°E	
	136/31°	037/74°E	
	129/27°	038/75°E	
	330/75°	024/80°E	
	325/77°	120/47°S	
	326/77°	096/62°S	
	141/53°	353/79°E	
	138/64°	170/27°W	
	141/59°	070/45°S	
	154/62°	210/32°W	
	144/67°	178/25°W	
	141/52°	212/84°W	
	157/84°	211/35°W	
	160/84°	162/88°W	
	155/82°	148/60°W	
	120/45°	069/54°S	
	126/36°	152/61°W	
	126/38°	163/52°W	
	084/26°	155/36°W	
	086/28°	232/49°N	
	090/20°	324/66°E	
	084/30°	329/62°E	
	072/30°	331/32°E	
	100/26°	323/48°E	
	147/44°	331/66°E	
	153/45°	054/51°S	
	140/44°	321/58°E	
	148/80°	074/59°S	
	146/74°	140/69°W	
	150/65°		
	144/66°		
	142/76°		
	143/75°		
	146/80°		
	145/65°		
	149/60°		
	144/59°		
	131/35°		
	139/42°		
	150/56°		
	149/54°		
	151/45°		

	148/46°		
Zone 3	140/33°	233/6°N	130/60°S
	145/32°	326/37°E	126/67°S
	136/27°	336/85°E	147/57°W
	120/17°	180/45°W	
	100/25°	065/79°S	
	185/16°	035/50°E	
	154/48°	200/74°W	
	139/58°	065/86°S	
	150/49°	061/80°S	
	153/45°	220/45°W	
	122/36°	164/46°W	
	140/36°	338/39°E	
	134/33°	338/20°E	

FIGURES

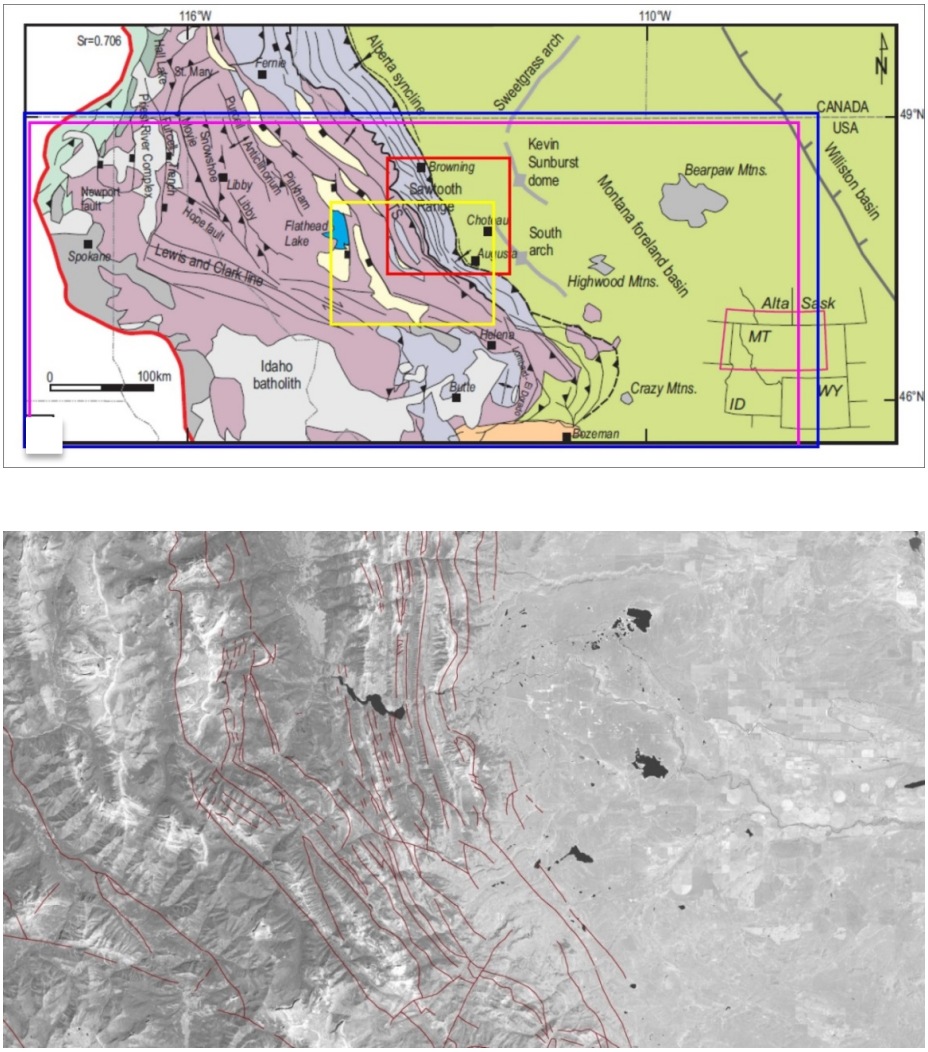

Figure 1 – (a) Regional tectonic-index map of northwestern Montana, approximate location of (1b) marked with red box (Fuentes et al., 2012), Figure 4 map view marked with yellow box, northern portion of Figure 5 marked with blue box, northern portion of Figure 6 marked with purple box. Noteworthy structures are the NW-SE trending Lewis Thrust System (LTS), the NW-SE trending Augusta Syncline, and the NW-SE trending Lewis and Clark Line; (b) satellite image depicting Sawtooth Range, MT (USGS.gov, 2015), note the Gibson Reservoir is the lake in the NW central portion. Fracture data is shown and indicated by red lines.

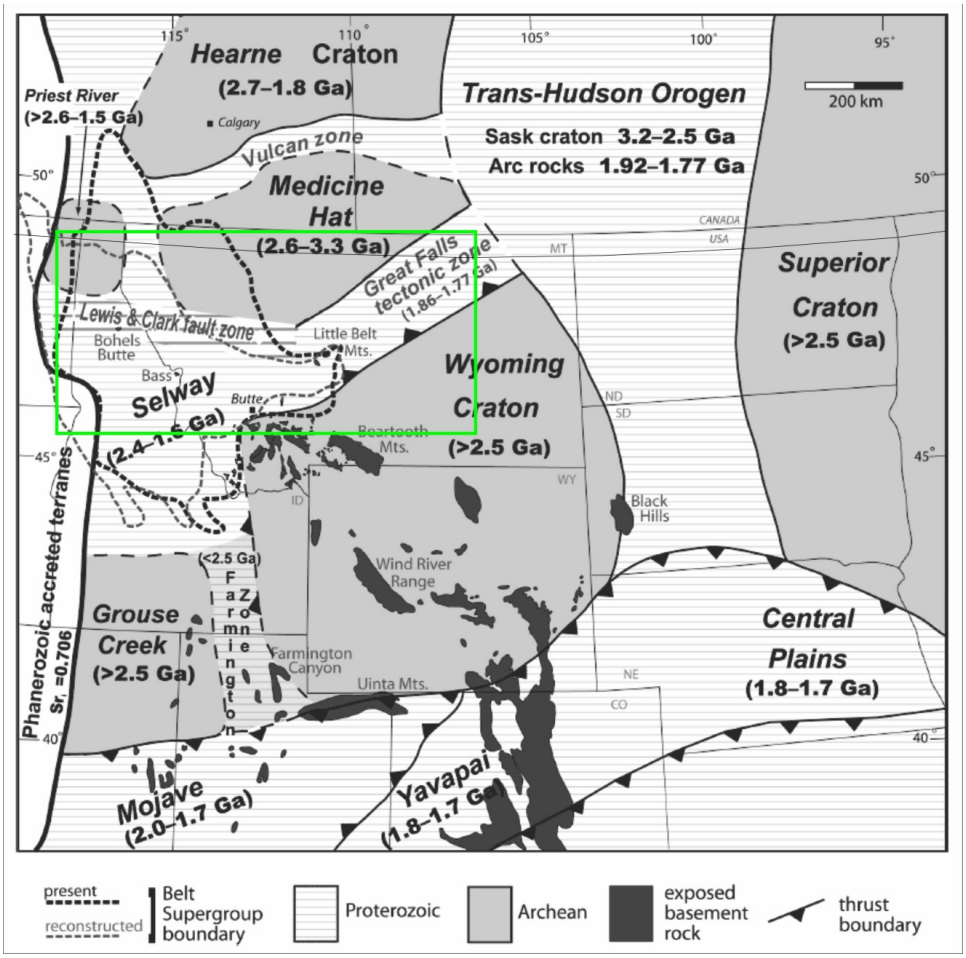

Figure 2 - Basement province map of northwestern Laurentia (Foster et al., 2006), with Figure 1a marked with green box. Figure shows the Wyoming Craton subducting under the Great Falls Tectonic Zone (a suture zone later reactivated as a shear zone), which is also subducting beneath the Medicine Hat Craton. This indicates the most probable basement configuration for the study area.

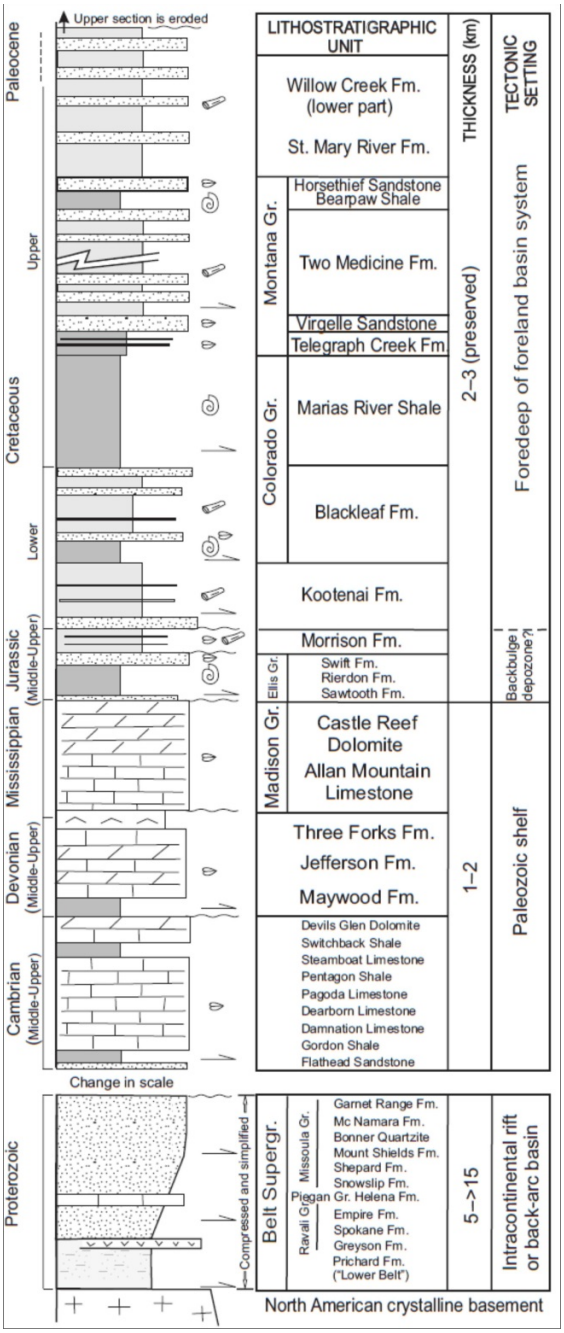

Figure 3 - Simplified stratigraphic log of northwestern Montana taken from Fuentes et al. (2012). Rocks identified in the study area range from the Cambrian (Flathead Sandstone) to the middle Jurassic (Morrison Formation).

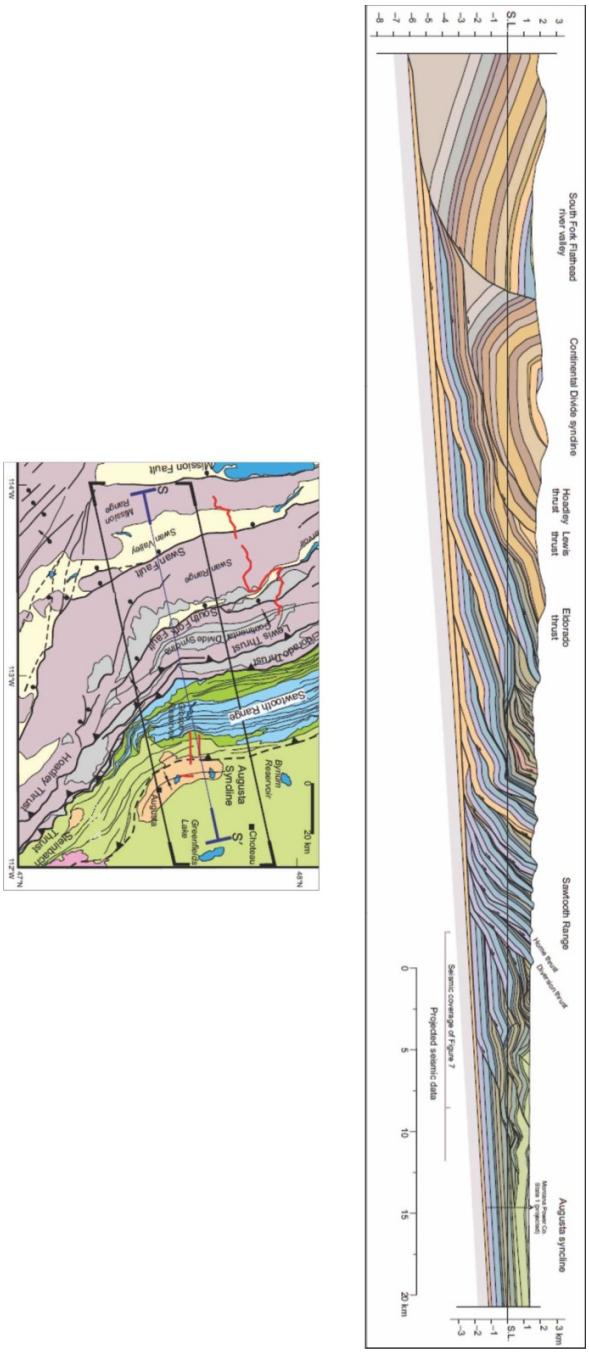

Figure 4 - Cross-section and map view of Sawtooth Range as depicted by Fuentes et al. (2012). Note the shallow, "thin-skinned" deformation of the Sawtooth Range. The western portion underwent large-scale subsidence, leading to greater initial taper, thinning as you travel east along the wedge.

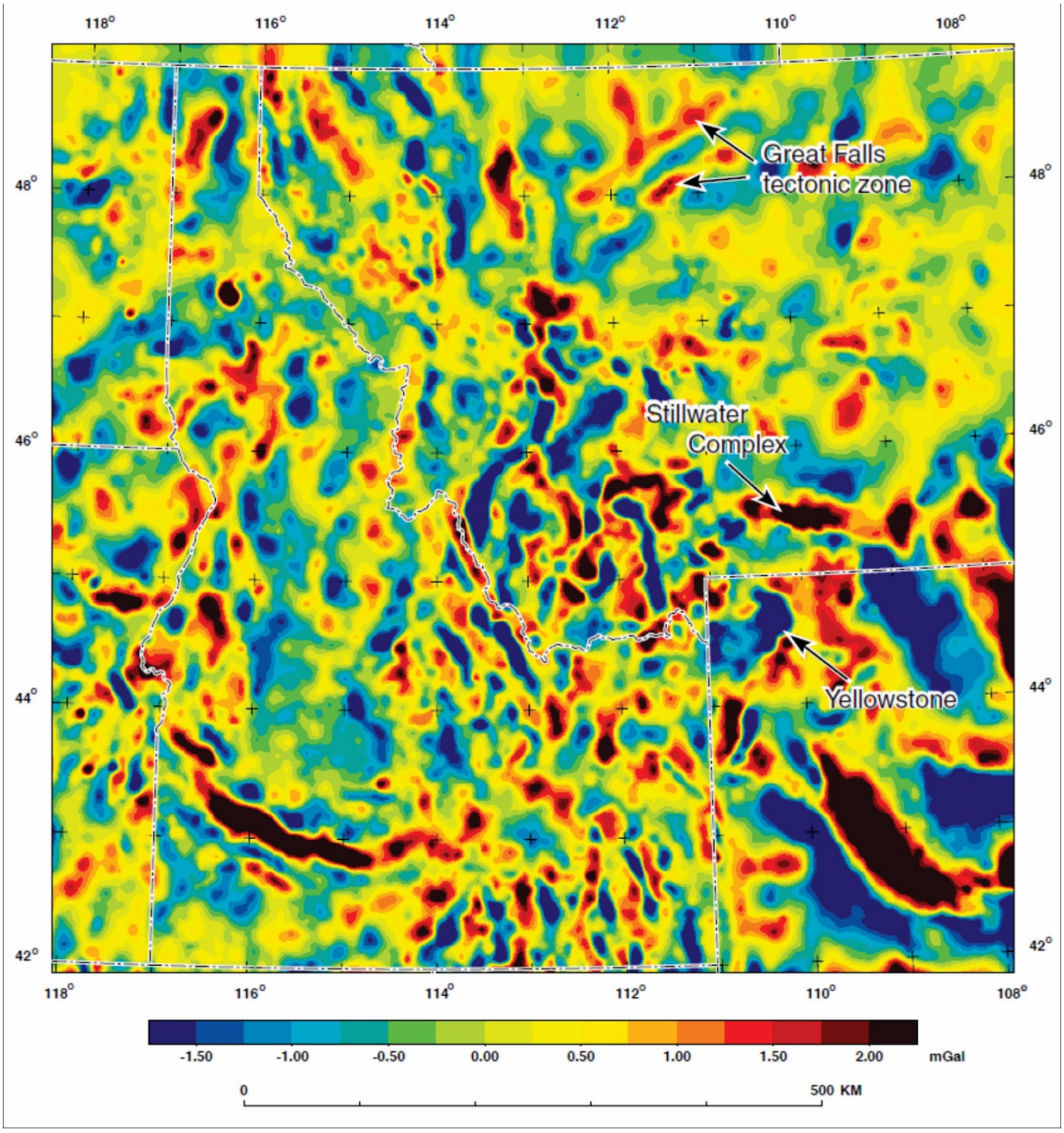

Figure 5 - Intermediate Wavelength Iso-Residual Gravity map (Mankinen et al., 2004). Strong lineations are noted in the northern portion (near Sawtooth Range) and is noted by Mankinen et al. (2004) to represent the Great Falls Tectonic Zone. The resolution is not high enough to determine the exact location of the Scapegoat-Bannatyne trend, however we believe it is the portion of the GFTZ responsible for fault orientation and geometric changes in the study area.

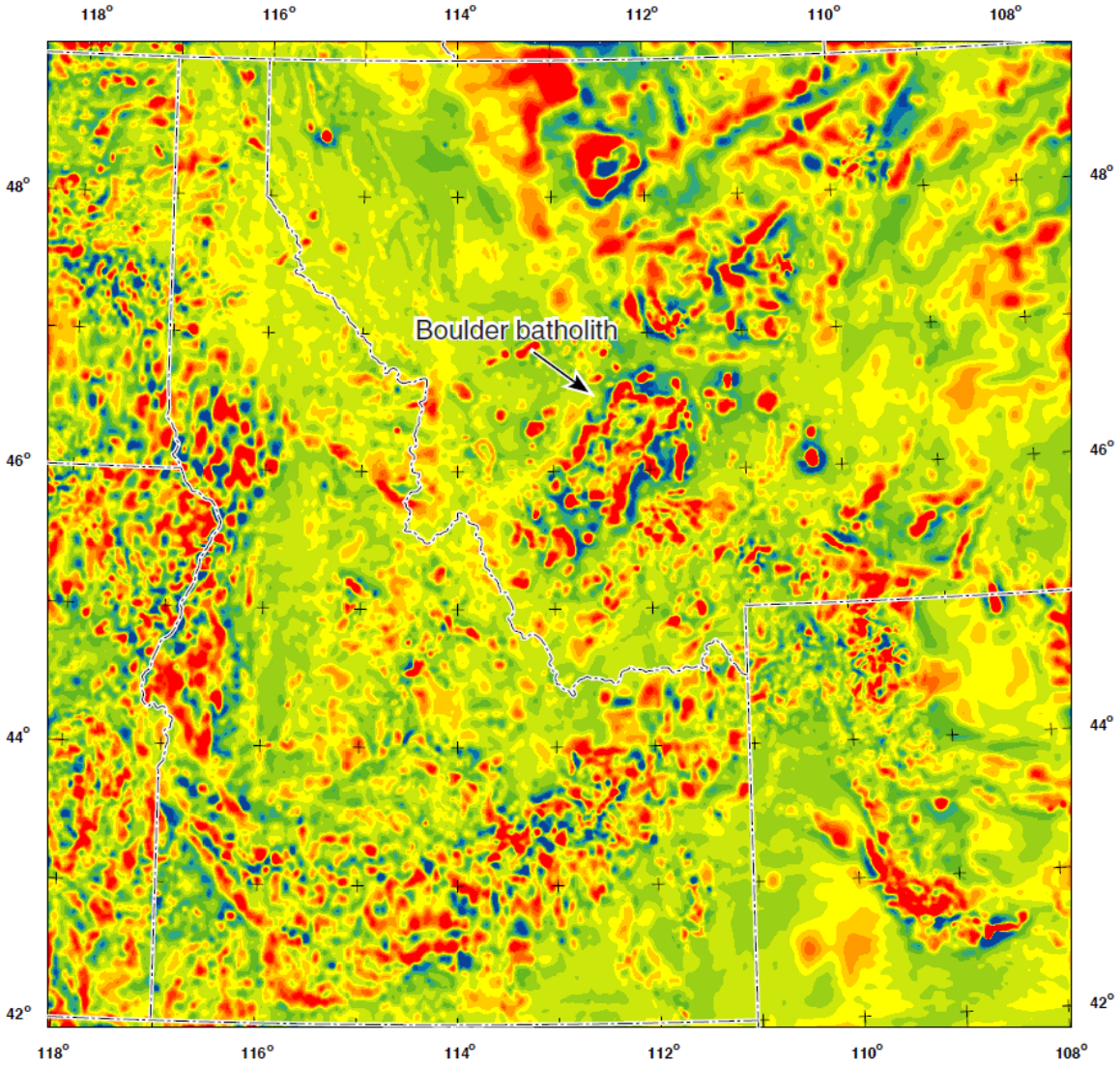

Figure 6 - Intermediate Wavelength Magnetic Potential map (Mankinen et al., 2004). Similar to Figure 5, there are strong lineations in the northern portion near the Sawtooth Range. This is also believed to indicate the location of the Great Falls Tectonic Zone. Once again resolution is not high enough to identify the Scapegoat-Bannatyne trend.

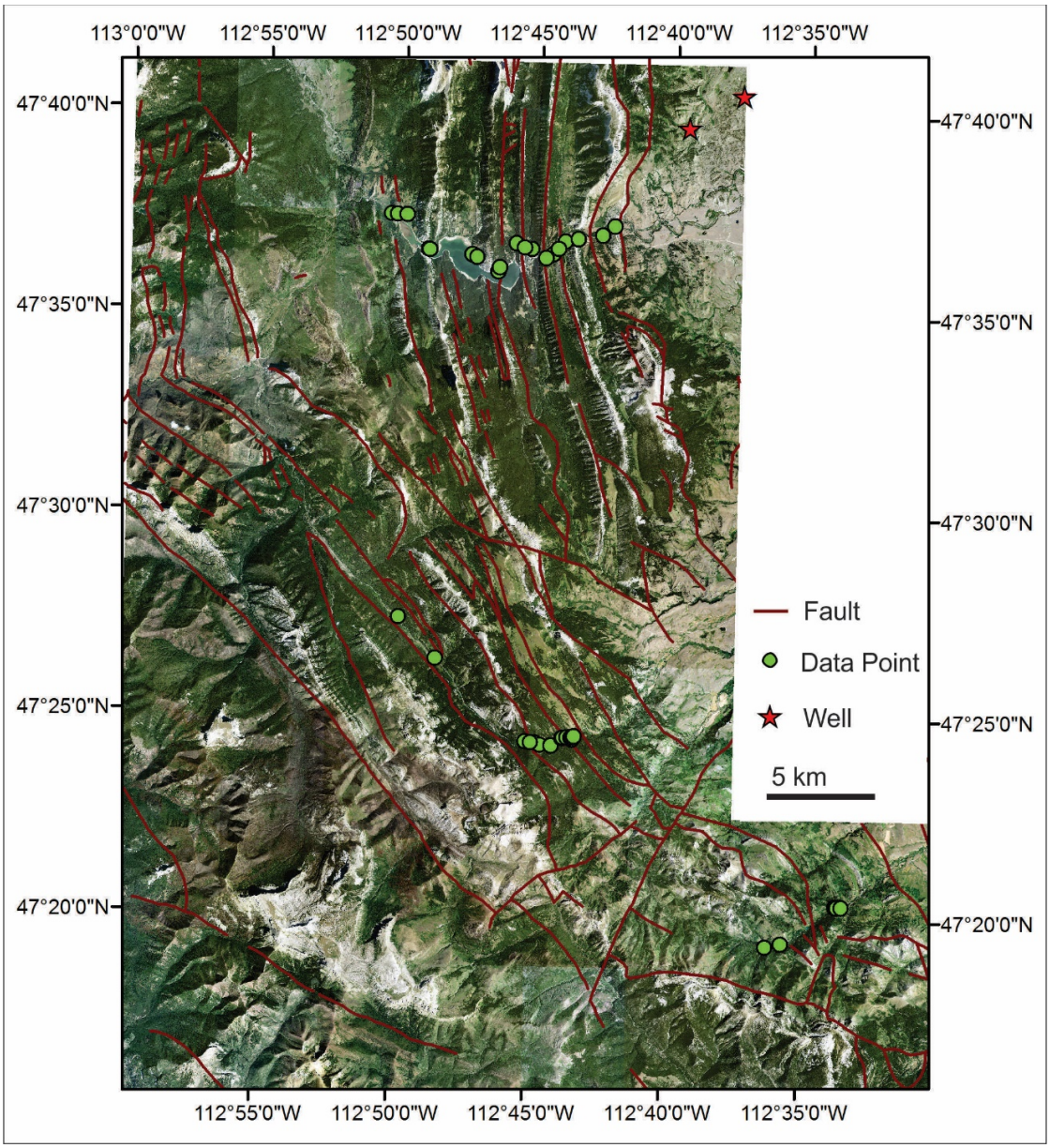

Figure 7 - Aerial map of study locations and faulting (USGS.gov, 2015). Faults have been indicated by red lines and data collection points are marked by green dots. Note the N-S fault trends around the Gibson Reservoir in the north. This orientation becomes more NW-SE in the central portion and then returns to a similar N-S trend in the southern portion. These changes in orientations are most likely influenced by a NE-SW trending basement structure (the Scapegoat-Bannatyne arm of the GFTZ).

FIGURE 8 – Analog Sandbox Model Setup

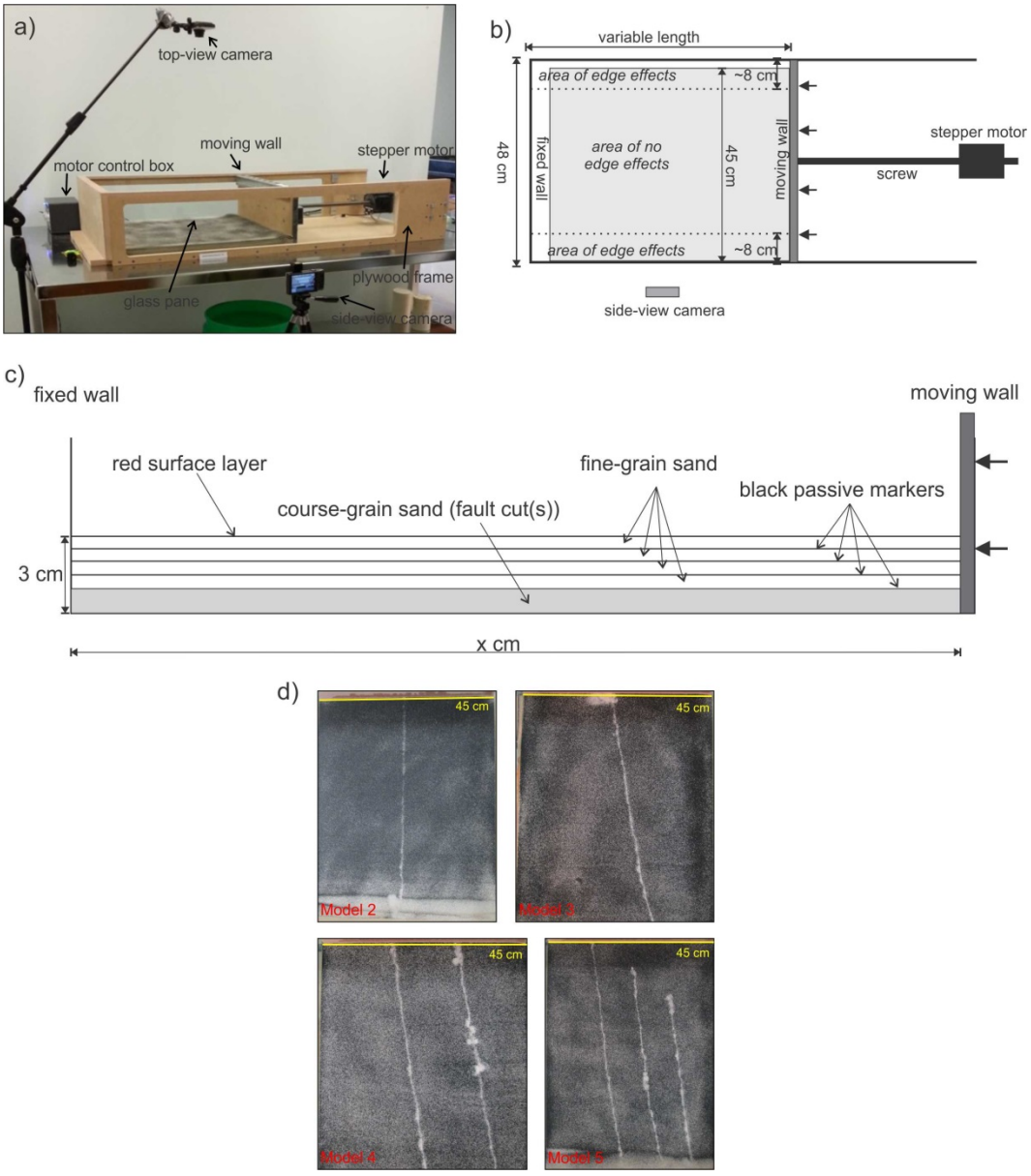

Figure 8 - Laboratory model setup modified from Burberry, 2015. (a) Labeled oblique-view photograph of modeling apparatus, with an experiment running. (b) plan-view diagram of the apparatus showing the areas where edge-effects are present and the area used for analysis in the center of the model. (c) Diagram of initial model configuration used in this study, with dimensions. (d) Locations of initial basement layer fault cuts in Models 2-5 (not to scale, moving wall at top of images).

FIGURE 9 – Basement Lineations

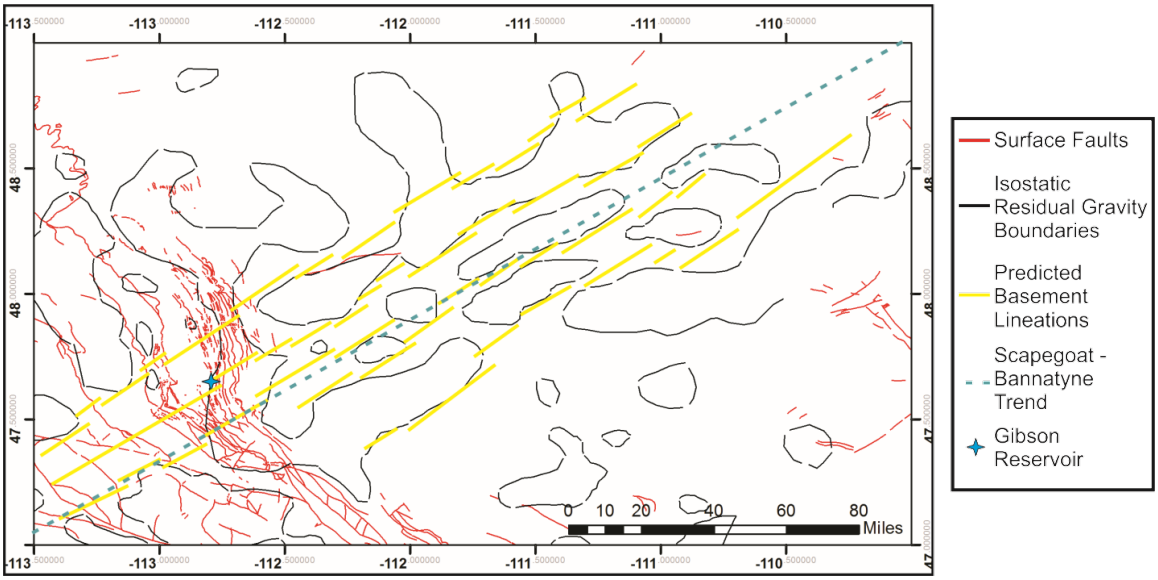

Figure 9 - Map of basement lineations constructed in ArcGIS. The surface faults have been marked with red lines and isostatic residual gravity boundaries have been marked with black lines. These boundaries show 3-4 strong lineations cross through the Sawtooth Range (Gibson Reservoir marked with blue cross). The potential trend of these basement lineations have been marked by yellow lines. We believe these lineations are parts of the Scapegoat-Bannatyne trend (approximate trend marked by the blue dashed line)

FIGURE 10.1 – Zone 1 Bedding and Fracture Data

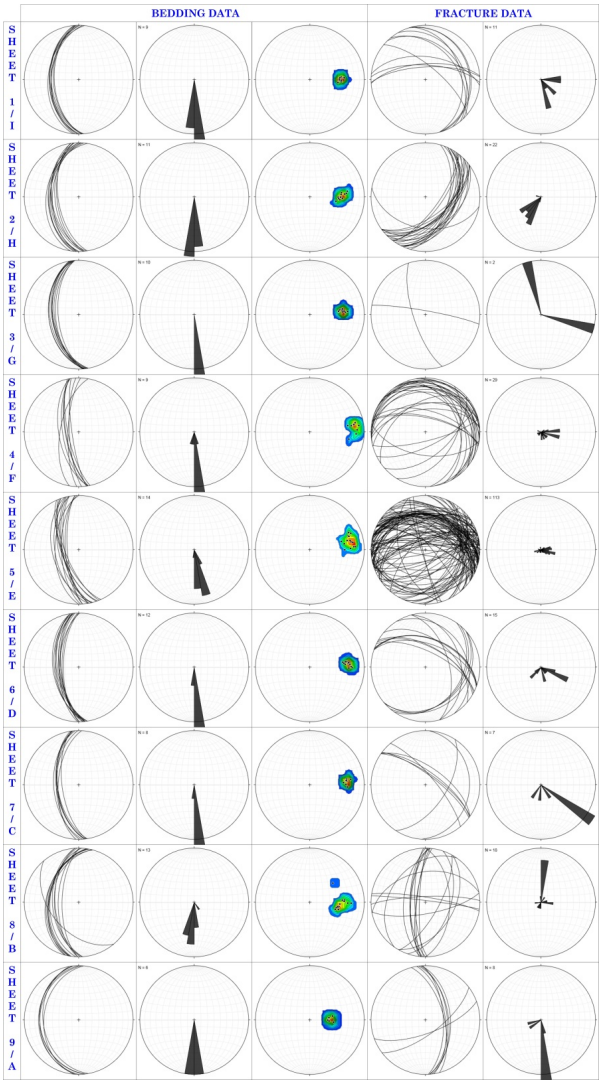

Figure 10.1 - Zone 1 bedding plane and pole data, as well as Zone 1 fracture plane and pole data, displayed as stereonets and rose diagrams. The individual thrust sheets (Sheet 1-I to Sheet 9-A) make up the rows. The first column shows the bedding plane orientation data (based on right-hand rule (RHR)). The second column displays the bedding plane data in rose diagram form to indicate primary bedding plane orientations (RHR). The third column displays the poles to bedding planes contoured to indicate cluster. The fourth column shows the fracture plane orientation data. The fifth column displays the fracture orientation data in rose diagram form to indicate primary fracture orientations. Strike of bedding planes and fractures are given by one end only unless explicitly stated otherwise.

FIGURE 10.2 – Zone 1 Rotated Fracture Data

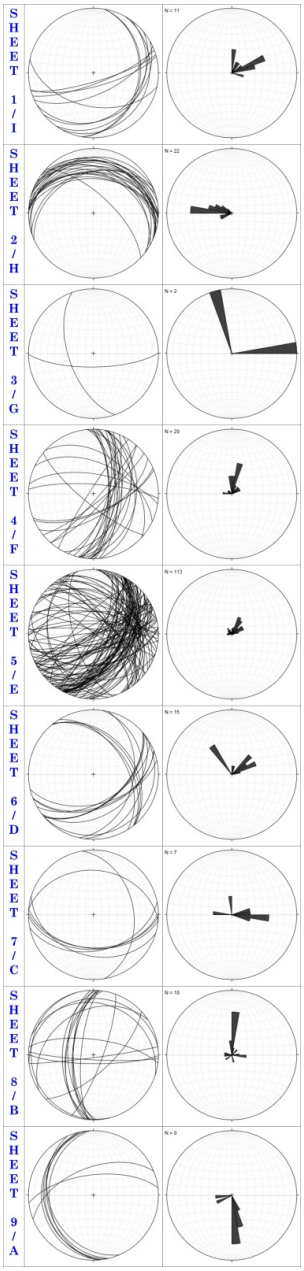

Figure 10.2 - Zone 1 fracture data rotated to horizontal displayed as stereonets and rose diagrams. The individual thrust sheets (Sheet 1-I to Sheet 9-A) make up the rows. The first column shows the rotated fracture plane orientation data. The second column displays the rotated fracture orientation data in rose diagram form to indicate primary rotated fracture orientations. Strike of bedding planes and fractures are given by one end only unless explicitly stated otherwise.

FIGURE 10.3 – Zone 2 Bedding and Fracture Data

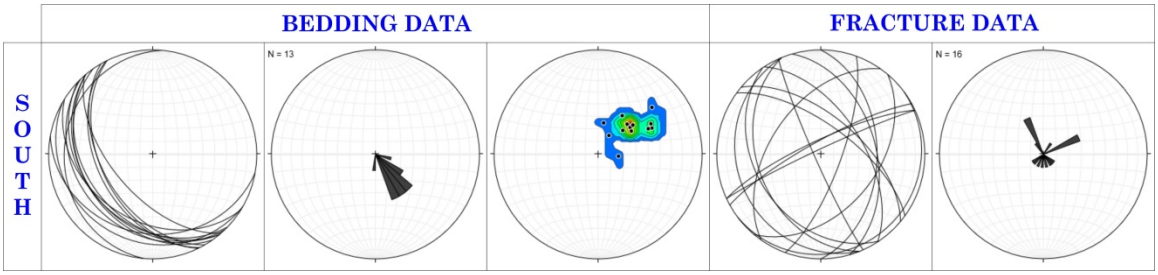

Figure 10.3 - Zone 2 bedding plane and pole data, as well as Zone 2 fracture plane and pole data, displayed as stereonets and rose diagrams. The first column shows the bedding plane orientation data (based on right-hand rule (RHR)). The second column displays the bedding plane data in rose diagram form to indicate primary bedding plane orientations (RHR). The third column displays the poles to bedding planes contoured to indicate cluster. The fourth column shows the fracture plane orientation data. The fifth column displays the fracture orientation data in rose diagram form to indicate primary fracture orientations. Strike of bedding planes and fractures are given by one end only unless explicitly stated otherwise.

FIGURE 10.4 – Zone 2 Rotated Fracture Data

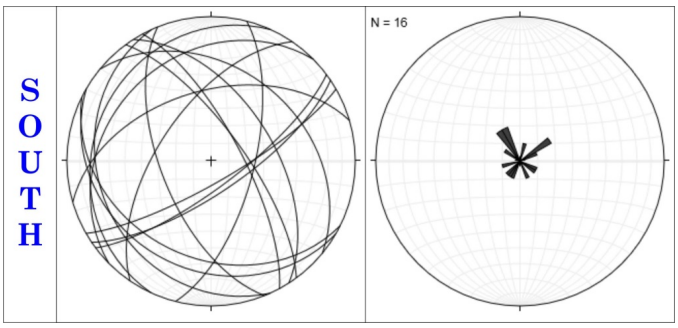

Figure 10.4 - Zone 2 fracture data rotated to horizontal displayed as stereonets and rose diagrams. The first column shows the rotated fracture plane orientation data. The second column displays the rotated fracture orientation data in rose diagram form to indicate primary rotated fracture orientations. Strike of bedding planes and fractures are given by one end only unless explicitly stated otherwise.

FIGURE 10.5 – Zone 3 Bedding and Fracture Data

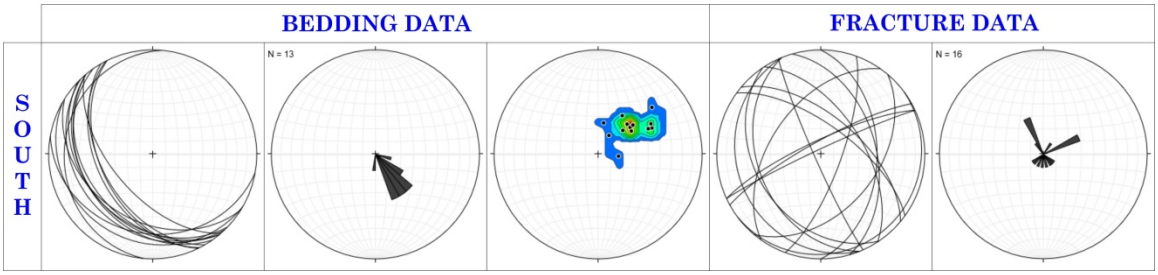

Figure 10.5 - Zone 3 bedding plane and pole data, as well as Zone 3 fracture plane and pole data, displayed as stereonets and rose diagrams. The first column shows the bedding plane orientation data (based on right-hand rule (RHR)). The second column displays the bedding plane data in rose diagram form to indicate primary bedding plane orientations (RHR). The third column displays the poles to bedding planes contoured to indicate cluster. The fourth column shows the fracture plane orientation data. The fifth column displays the fracture orientation data in rose diagram form to indicate primary fracture orientations. Strike of bedding planes and fractures are given by one end only unless explicitly stated otherwise.

FIGURE 10.6 – Zone 3 Rotated Fracture Data

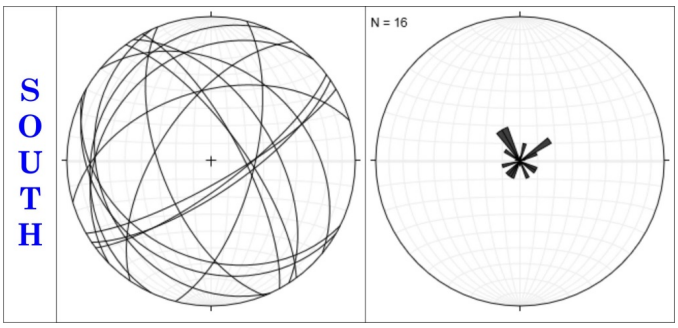

Figure 10.6 - Zone 3 fracture data rotated to horizontal displayed as stereonets and rose diagrams. The first column shows the rotated fracture plane orientation data. The second column displays the rotated fracture orientation data in rose diagram form to indicate primary rotated fracture orientations. Strike of bedding planes and fractures are given by one end only unless explicitly stated otherwise.

FIGURE 11 – Sandbox Model 1

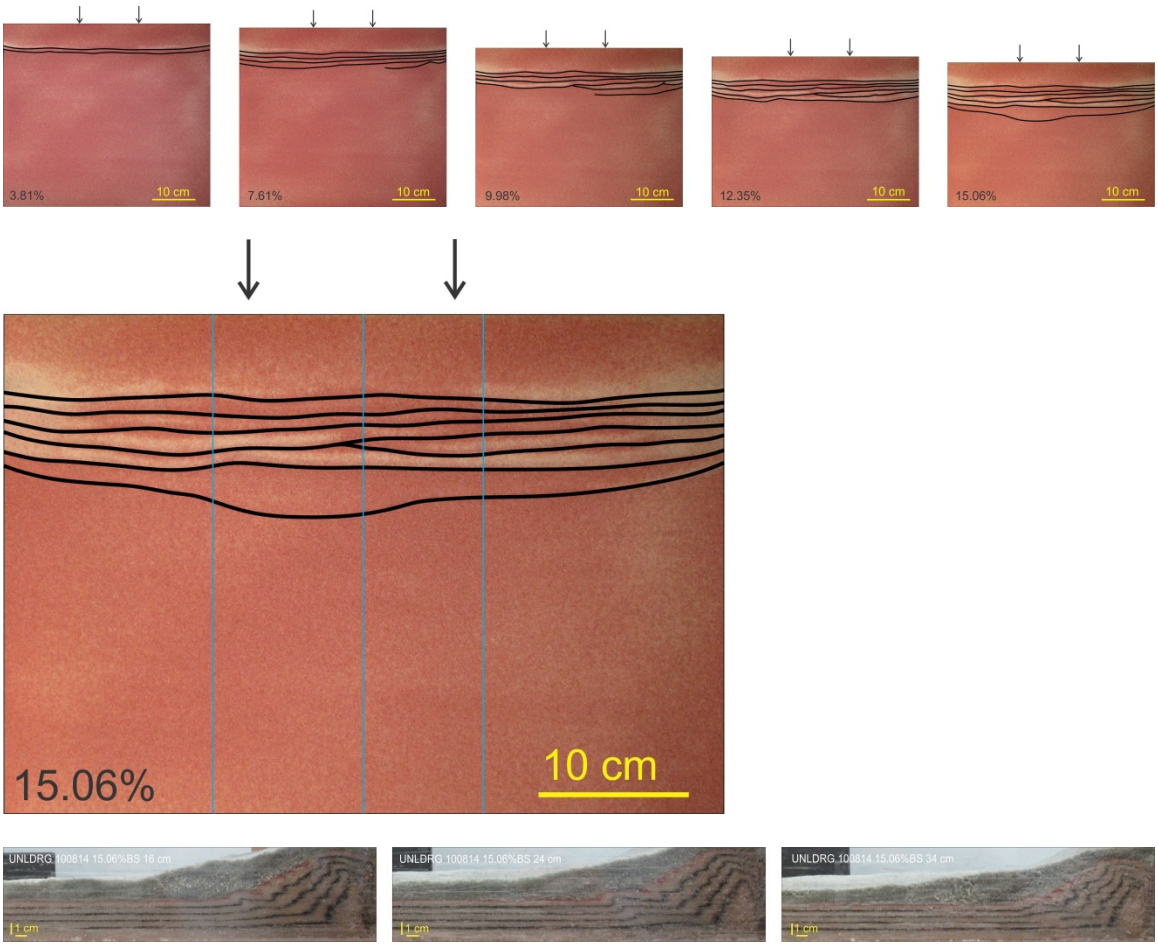

Figure 11 - Analog Model 1 (UNLDRG 100814) serving as a control model. (a) Surface images depicting various bulk shortenings (shortening increases left to right, maximum 15.06%). Black lines indicate thrust faults, black arrows indicate compression direction. Note that faulting propagates uniformly across surface. (b) Surface image indicating cross-section locations (blue lines). Black lines indicate thrust faults, black arrows indicate compression direction. Note uniform fault orientation trend. (c) Cross-sections indicating a stacked thrust system with uniform geometries.

FIGURE 12 – Sandbox Model 2

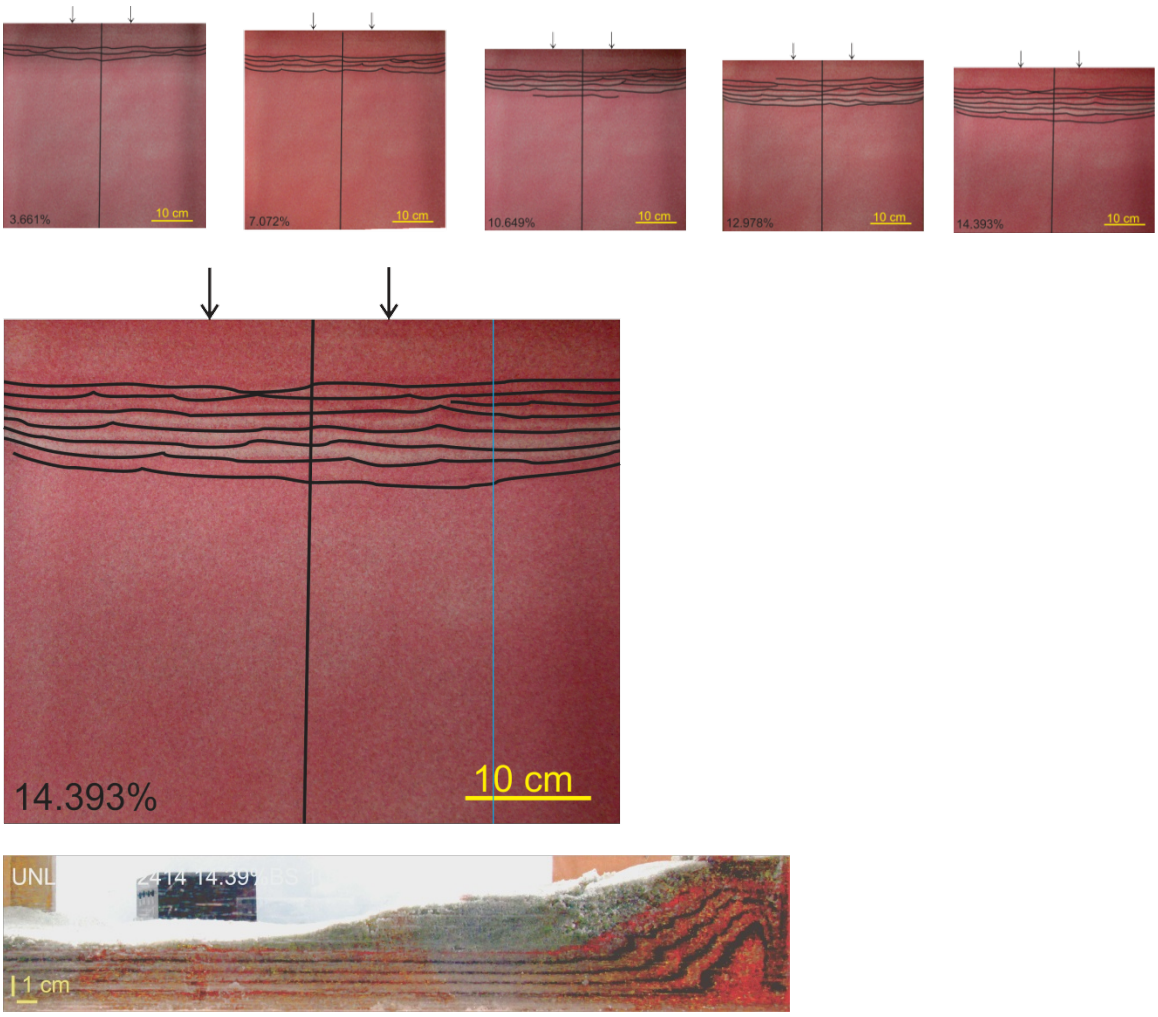

Figure 12 - Analog Model 2 (UNLDRG 102414) with a single basement fault cut perpendicular to compression direction. (a) Surface images depicting various bulk shortenings (shortening increases left to right, maximum 14.393%). Black lines indicate thrust faults, black arrows indicate compression direction, vertical black line indicates basement cut. Note that faulting originated above basement cut and propagated outwards. (b) Surface image indicating cross-section locations (blue line). Black lines indicate thrust faults, black arrows indicate compression direction, vertical black line indicates basement cut. Note fault orientation trend is still uniform, similar to Model 1. (c) Cross-sections indicating a stacked thrust system with uniform geometries, similar to Model 1.

FIGURE 13 – Sandbox Model 3

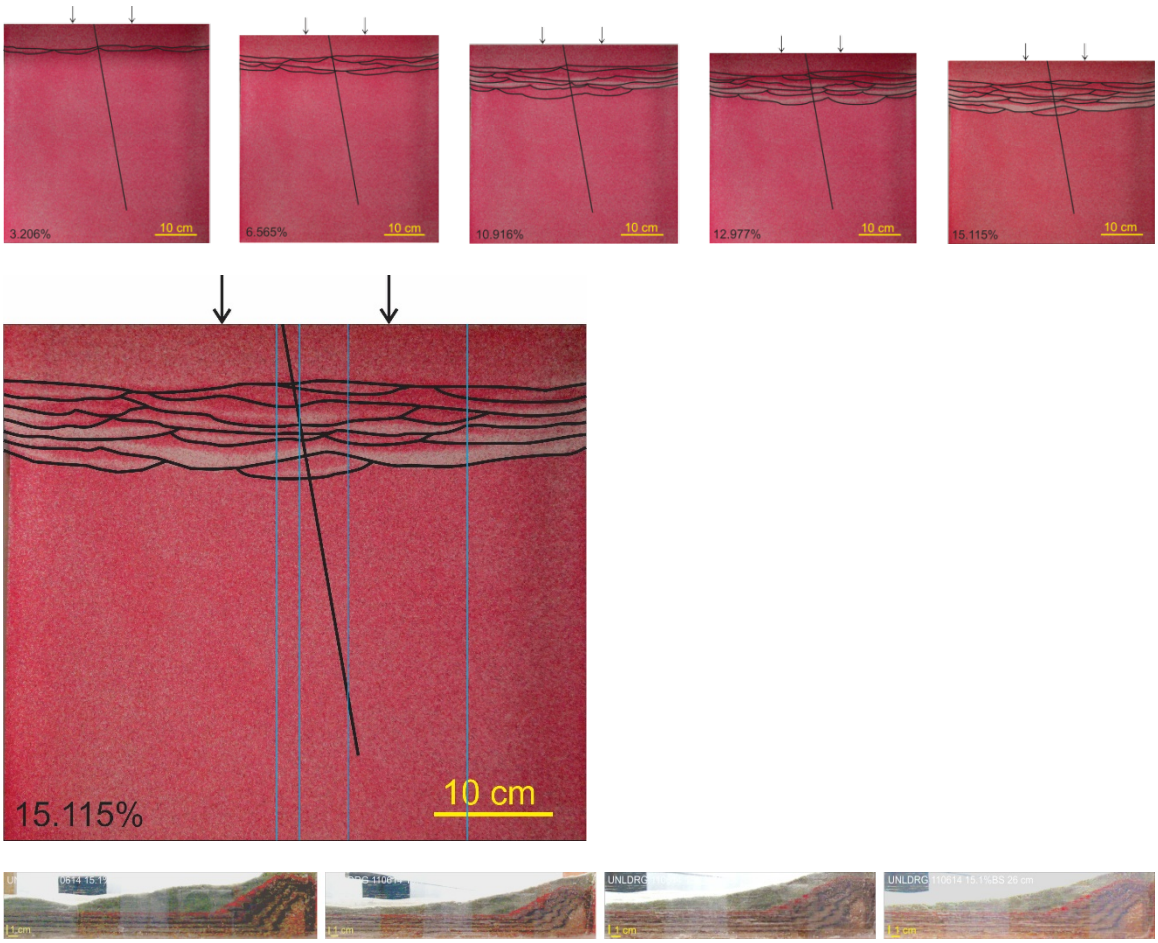

Figure 13 - Analog Model 3 (UNLDRG 110614) with a single basement fault cut offset to compression direction. (a) Surface images depicting various bulk shortenings (shortening increases left to right, maximum 15.115%). Black lines indicate thrust faults, black arrows indicate compression direction, NW-SE black line indicates basement cut. Note that faulting originated above basement cut and propagated outward, with segmenting occurring. (b) Surface image indicating cross-section locations (blue lines). Black lines indicate thrust faults, black arrows indicate compression direction, NW-SE black line indicates basement cut. Note variations in fault orientation trend and fault segments. (c) Cross-sections indicating significant changes. End result is a stacked thrust system with geometries that change traveling across the basement cut.

FIGURE 14 – Sandbox Model 4

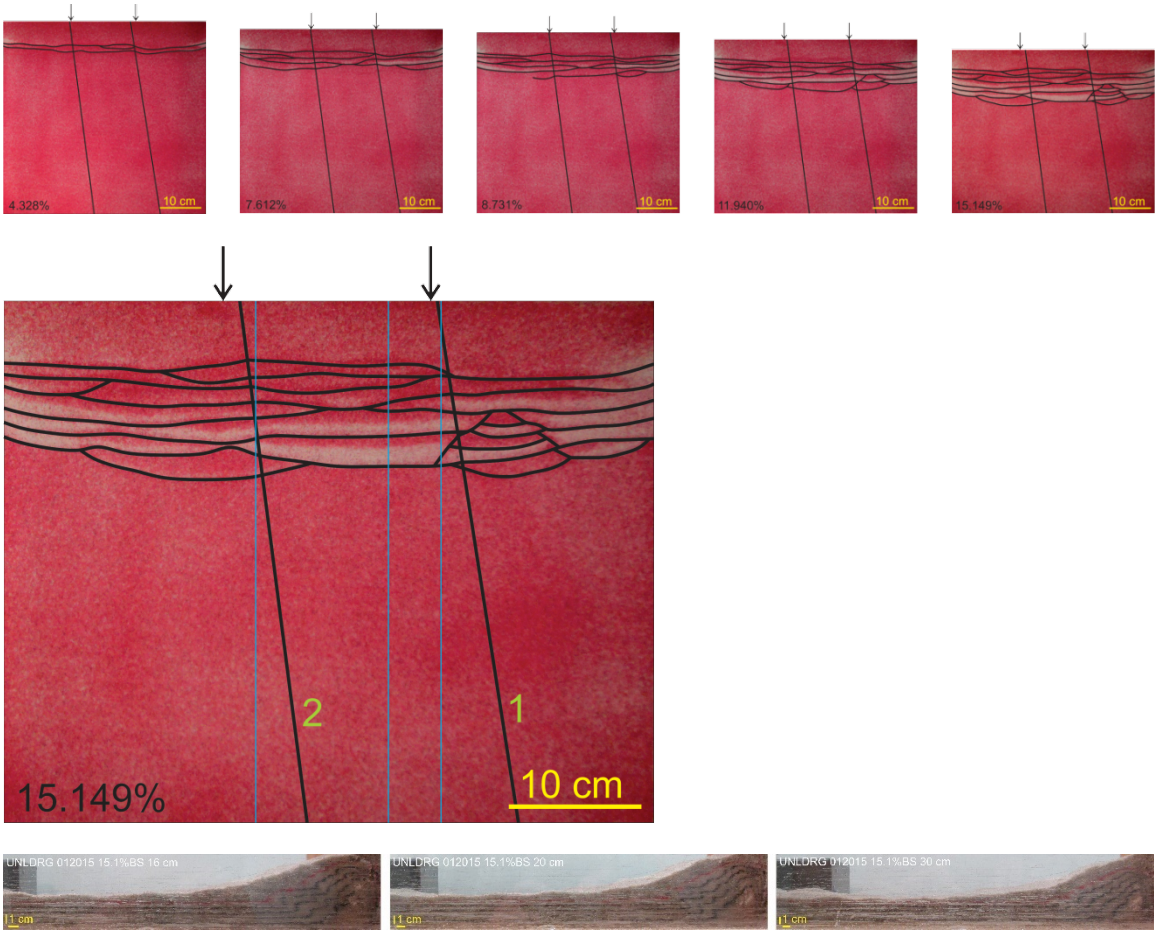

Figure 14 - Analog Model 4 (UNLDRG 012015) with two parallel basement faults cut perpendicular to compression direction. (a) Surface images depicting various bulk shortenings (shortening increases left to right, maximum 15.149%). Black lines indicate thrust faults, black arrows indicate compression direction, NW-SE black lines indicate basement cuts. Note that faulting originated above basement cuts and propagated outward, with segmenting occurring. (b) Surface image indicating cross-section locations (blue lines). Black lines indicate thrust faults, black arrows indicate compression direction, NW-SE black lines indicate basement cuts. Note variations in fault orientation trend and fault segments. (c) Cross-sections indicating significant changes. End result is a stacked thrust system with geometries that change traveling across the basement cuts.

FIGURE 15 – Sandbox Model 5

Figure 15 - Analog Model 5 (UNLDRG 050815) with three parallel *en echelon* basement faults cut perpendicular to compression direction. (a) Surface images depicting various bulk shortenings (shortening increases left to right, maximum 15.038%). Black lines indicate thrust faults, black arrows indicate compression direction, NW-SE black lines indicate basement cuts. Note that faulting originated above leftmost basement cut and propagated outward, with segmenting occurring (b) Surface image indicating cross-section locations (blue lines). Black lines indicate thrust faults, black arrows indicate compression direction, NW-SE black lines indicate basement cuts. Note variations in fault orientation trend and fault segments. (c) Cross-sections indicating significant changes. End result is a stacked thrust system with geometries that change traveling across the basement cuts.

FIGURE 16 – Aerial Map with Interpretations

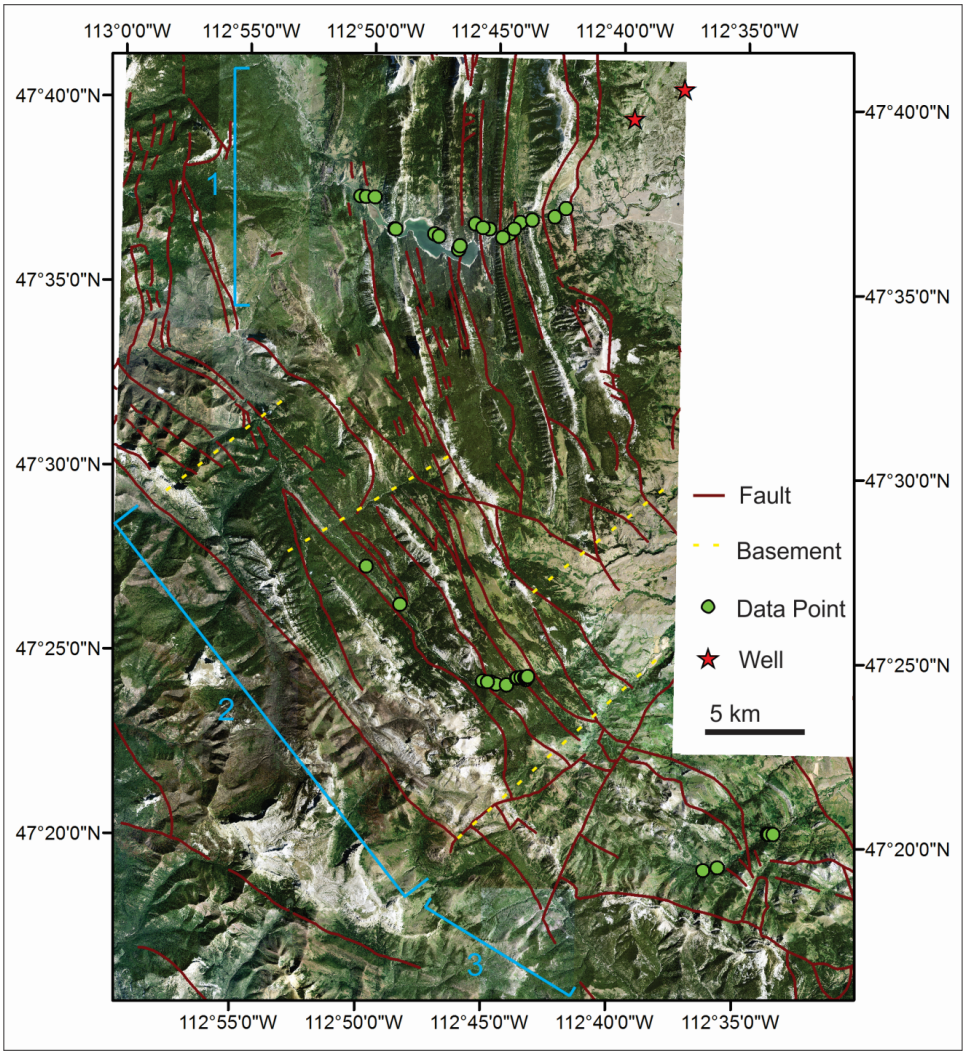

Figure 16 - Aerial photo with definitive deformation zones marked (1-3), and most plausible trends of basement faulting marked. (USGS.gov, 2015). The primary factor determining the deformation zones is changes in fault orientations. The trend of the northern area (Zone 1) is N-S, the trend of the central zone (Zone 2) is NW-SE, and the trend of the southern zone (Zone 3) returns to that of N-S. We believe this is caused by multiple arms of the Scapegoat-Bannatyne trend extending through the region (marked by yellow dashed lines). The orientation changes would occur wherever a new arm was encountered.

FIGURE 17 – Model 1 Interpretations

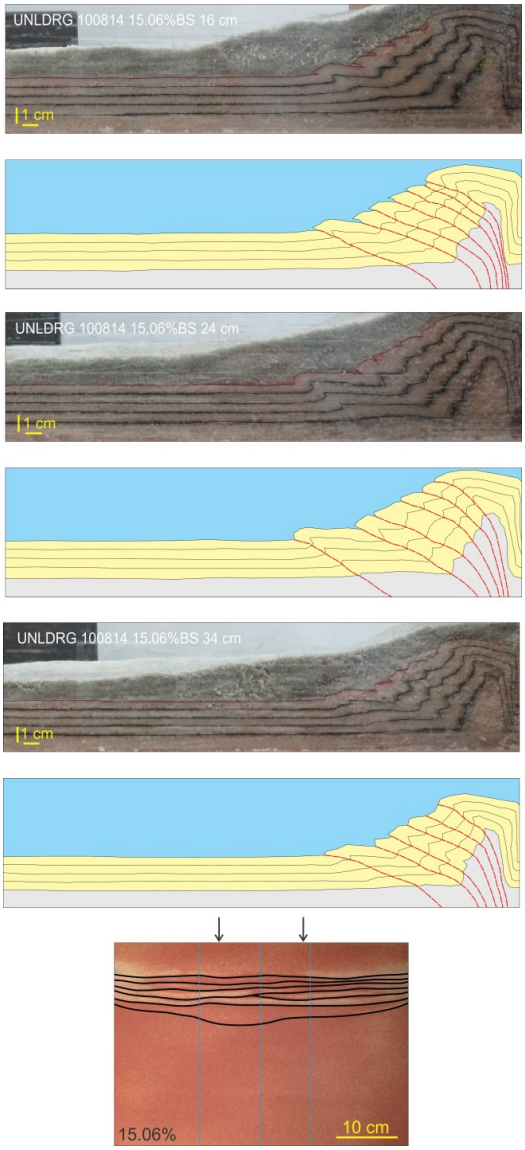

Figure 17 - Analog Model 1 (UNLDRG100814) cross section interpretations and top view indicating corresponding locations (blue lines). Black lines indicate thrust faults, black arrows indicate compression direction. Cross section cut depth increases in images top to bottom (right to left on top view). Overlays follow their corresponding cross section. Thrusts marked with dotted red lines. Model exhibited even fault propagation on the surface, resulting an evenly spaced imbricate thrust stack with little variation in surface trend and basement dip.

FIGURE 18 - Model 2 Interpretations

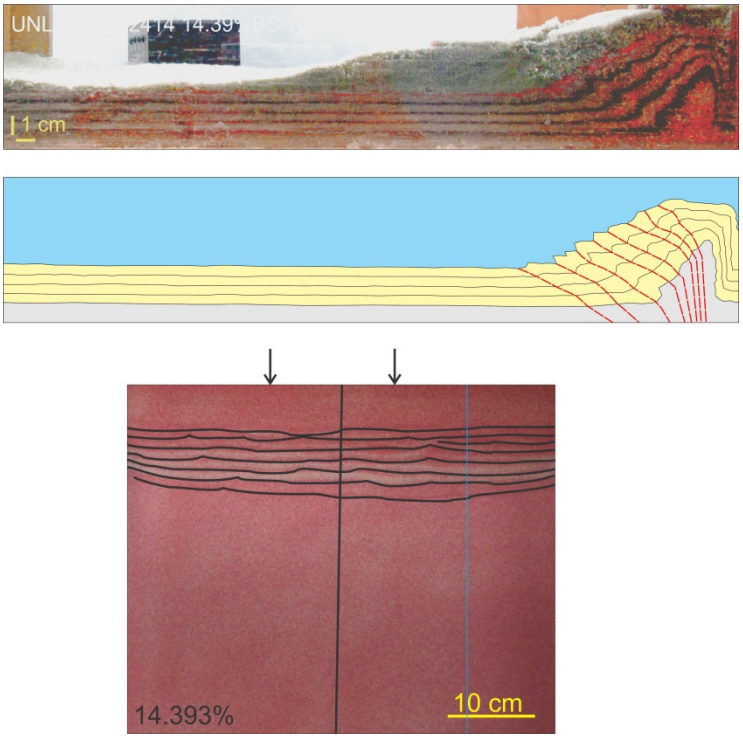

Figure 18 - Analog Model 2 (UNLDRG102414) cross section interpretations and top view indicating corresponding locations (blue line). Black lines indicate thrust faults, black arrows indicate compression direction, vertical black line indicates basement cut. Cross section cut depth increases in images top to bottom (right to left on top view). Overlays follow their corresponding cross section. Thrusts marked with dotted red lines. Model 2 developed similar to Model 1, however surface faults originated above basement cuts and propagated outwards (most likely due to an increase in resistance cause by the basement cut). The result was an evenly spaced imbricate thrust stack with little change in surface trend and basement dip, similar to Model 1.

FIGURE 19 – Model 3 Interpretations

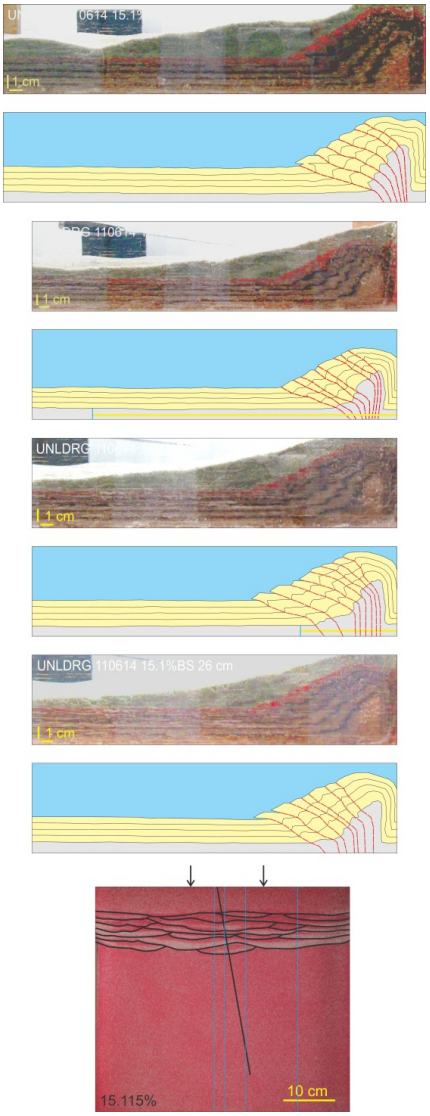

Figure 19 - Analog Model 3 (UNLDRG110614) cross section interpretations and top view indicating corresponding locations (blue lines). Black lines indicate thrust faults, black arrows indicate compression direction, NW-SE black line indicates basement cut. Cross section cut depth increases in images top to bottom (right to left on top view). Overlays follow their corresponding cross section. Thrusts marked with dotted red lines. Fault propagation was similar to Model 2, originating above basement cuts and propagating outwards. Final surface fault trends were segmented. The imbricate thrust stack also exhibited closer spacing as the proximity to the basement cut increased.

FIGURE 20 – Model 4 Interpretations

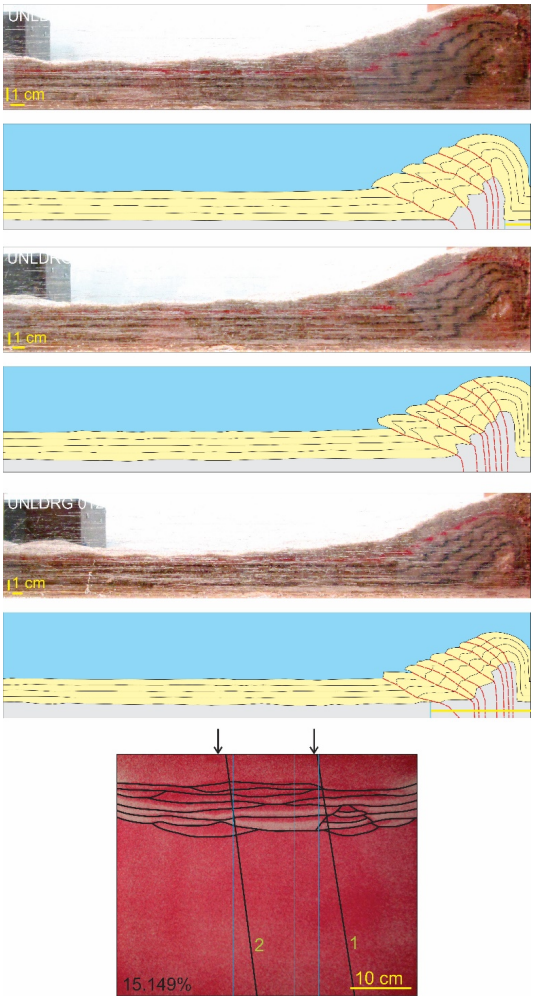

Figure 20 - Analog Model 4 (UNLDRG012015) cross section interpretations and top view indicating corresponding locations (blue lines). Black lines indicate thrust faults, black arrows indicate compression direction, NW-SE black lines indicate basement cuts. Cross section cut depth increases in images top to bottom (right to left on top view). Overlays follow their corresponding cross section. Thrusts marked by dotted red lines. Fault propagation was similar to Models 2 & 3, originating above basement cuts and propagating outwards. Segmenting in the surface faults was greater than in Model 3. Additional faulting oblique to surface trend also occurred. The imbricate thrust stack near basement cut 1 were steeply dipping and evenly spaced. The stack in between basement cuts 1 and 1 were more numerous, shallow dipping, and closely spaced. The stack near basement cut 2 were similar to the intermediate stack, yet steeper dipping.

FIGURE 21 – Model 5 Interpretations

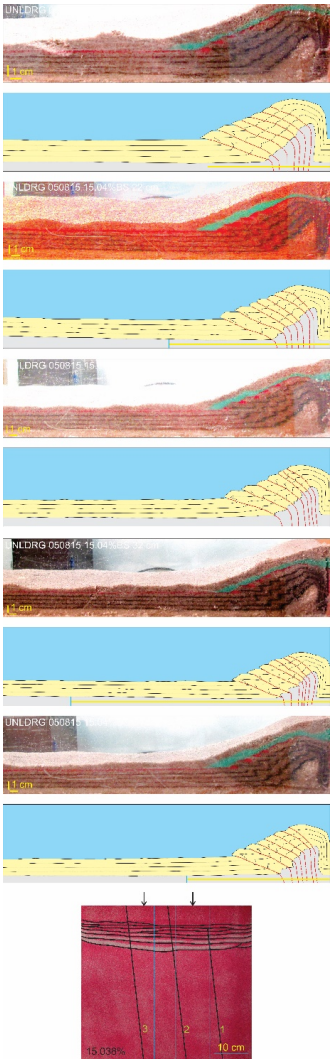

Figure 21 - Analog Model 5 (UNLDRG050815) cross section interpretations and top view indicating corresponding locations (blue lines). Black lines indicate thrust faults, black arrows indicate compression direction, NW-SE black lines indicate basement cuts. Cross section cut depth increases in images top to bottom (right to left on top view). Overlays follow their corresponding cross section. Thrusts marked by dotted red lines. Faulting originated above basement cut 3 and propagated outwards. Growth was more pronounced as basement cuts 1 and 2 became involved. Variations in surface trend and segmentation occurred at or between the basement fault cuts. The imbricate thrust stack near basement cuts 1 and 3 are shallow and steep, and the stack near basement cut 2 had more variation in the upper stack.

FIGURE 22 – Earthquake Map of Montana

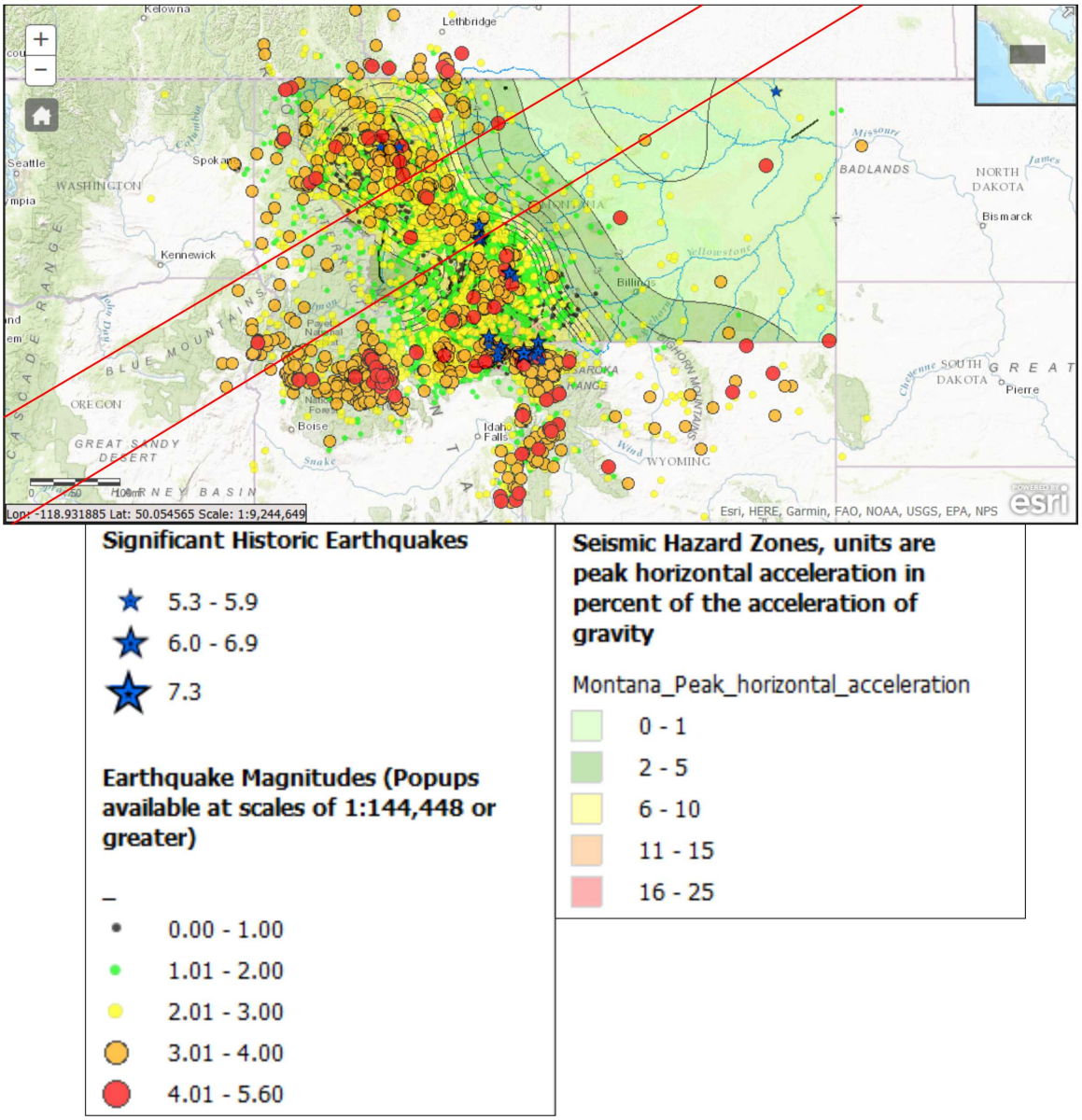

Figure 22 - Historical earthquake map of Montana and surrounding area with approximate location of GFTZ taken from Figure 2. This figure demonstrates how the Sawtooth Region is ideal for earthquake study and could benefit from advance warning systems. (http://data.mbmg.mtech.edu/mapper/mapper.asp?view=Quakes&)

FIGURE 23 – Hydrocarbon Fields Northwestern Montana

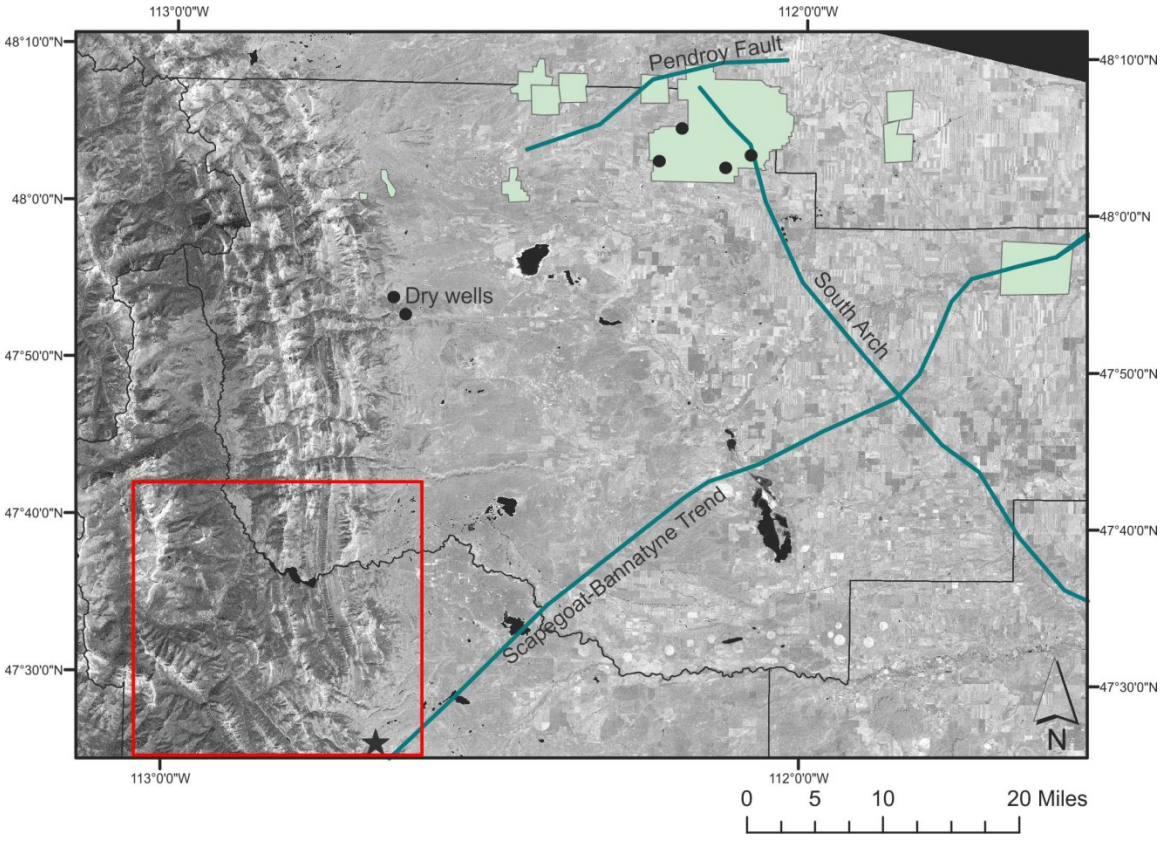

Figure 23 - Hydrocarbon field map of northwestern Montana with basement faults, northern part of study area marked in red box. Wells are marked with black dots, fields in green, faults in blue (Note small fields right along Sawtooth Range). Image created with data taken from the Montana Bureau of Oil and Gas. Figure demonstrates how large hydrocarbon fields along basement faults in the Sawtooth Region would enable further study for potential hydrocarbon migration along reactivated fault pathways.